

## HOMOGENEOUS *UGRIZ* PHOTOMETRY FOR ACS VIRGO CLUSTER SURVEY GALAXIES: A NON-PARAMETRIC ANALYSIS FROM SDSS IMAGING

CHIN-WEI CHEN<sup>1,2</sup>, PATRICK CÔTÉ<sup>2</sup>, ANDREW A. WEST<sup>3</sup>, ERIC W. PENG<sup>4,5</sup>, AND LAURA FERRARESE<sup>2</sup>

<sup>1</sup> Graduate Institute of Astronomy, National Central University, No. 300 Jungda Road, Taoyuan 32054, Taiwan; cwchen2014@gmail.com

<sup>2</sup> Herzberg Institute of Astrophysics, National Research Council of Canada, 5071 West Saanich Road, Victoria, BC V9E 2E7, Canada

<sup>3</sup> Department of Astronomy, Boston University, 725 Commonwealth Ave., Boston, MA 02215, USA

<sup>4</sup> Department of Astronomy, Peking University, Beijing 100871, China

<sup>5</sup> Kavli Institute for Astronomy and Astrophysics, Peking University, Beijing 100871, China

Received 2010 April 1; accepted 2010 August 31; published 2010 October 18

### ABSTRACT

We present photometric and structural parameters for 100 ACS Virgo Cluster Survey (ACSVCS) galaxies based on homogeneous, multi-wavelength (*ugriz*), wide-field SDSS (DR5) imaging. These early-type galaxies, which trace out the red sequence in the Virgo Cluster, span a factor of nearly  $\sim 10^3$  in *g*-band luminosity. We describe an automated pipeline that generates background-subtracted mosaic images, masks field sources and measures mean shapes, total magnitudes, effective radii, and effective surface brightnesses using a model-independent approach. A parametric analysis of the surface brightness profiles is also carried out to obtain Sérsic-based structural parameters and mean galaxy colors. We compare the galaxy parameters to those in the literature, including those from the ACSVCS, finding good agreement in most cases, although the sizes of the brightest, and most extended, galaxies are found to be most uncertain and model dependent. Our photometry provides an external measurement of the random errors on total magnitudes from the widely used Virgo Cluster Catalog, which we estimate to be  $\sigma(B_T) \approx 0.13$  mag for the brightest galaxies, rising to  $\approx 0.3$  mag for galaxies at the faint end of our sample ( $B_T \approx 16$ ). The distribution of axial ratios of low-mass (“dwarf”) galaxies bears a strong resemblance to the one observed for the higher-mass (“giant”) galaxies. The global structural parameters for the full galaxy sample—profile shape, effective radius, and mean surface brightness—are found to vary smoothly and systematically as a function of luminosity, with unmistakable evidence for changes in structural homology along the red sequence. As noted in previous studies, the *ugriz* galaxy colors show a nonlinear but smooth variation over a  $\sim 7$  mag range in absolute magnitude, with an enhanced scatter for the faintest systems that is likely the signature of their more diverse star formation histories.

**Key words:** galaxies: clusters: individual (Virgo) – galaxies: dwarf – galaxies: elliptical and lenticular, cD – galaxies: fundamental parameters

### 1. INTRODUCTION

Understanding the physical processes that shaped the structure of galaxies in the local universe remains a key goal in modern astrophysics. The past decade has seen significant progress toward an understanding of both the initial conditions that governed the hierarchical growth of structure and its evolution within a  $\Lambda$ CDM universe. At the same time, there is a growing realization that, because of the complex gas-dynamical processes involved in the formation of baryonic structures within merging dark matter halos, the “gastrophysical evolution” of galaxies is perhaps the most poorly understood stage of structure formation at the present time. It is for this reason that accurate and homogeneous data for nearby galaxies, which can be studied in a level of detail that will never be possible with high- $z$  systems, have taken on a renewed importance since they provide one of our few direct windows into the process of galaxy formation and evolution.

At a distance of  $D \approx 16.5$  Mpc (see Mei et al. 2007; Blakeslee et al. 2009 and references therein), the Virgo Cluster (Abell richness class = I and virial mass  $M_{200} \sim 4 \times 10^{14} M_\odot$ ; Girardi et al. 1995; McLaughlin 1999) is the nearest large collection of galaxies in the local universe, with virtually all morphological types represented in statistically significant numbers. For this reason, it has long played a central role in characterizing both the overall properties of galaxies and the fossil record of galaxy formation. Multi-wavelength observations of galaxies belonging to the Virgo Cluster have—and will continue—to play

a central role in a wide variety of topics focused on the general issues of galaxy formation and evolution, including galaxy scaling relations, the galaxy luminosity and mass functions, supermassive black holes in galaxies, active galactic nucleus feedback, the history of cosmic star formation, and the role of environment on galaxy evolution.

The most complete and homogeneous optical survey of the Virgo Cluster remains that of Binggeli et al. (1985), who used blue-sensitive photographic plates from the 2.5 m duPont telescope at Las Campanas observatory to survey a region of  $\sim 140$  deg $^2$  centered on the cluster core (usually taken to lie at, or near, M87=NGC4486=VCC1316, the cD galaxy that coincides with the peak of the X-ray gas emission; e.g., Böhringer et al. 1994). Their Virgo Cluster Catalog (VCC) consists of 2096 galaxies ranging from  $B_T \approx 9.3$  mag down to  $\approx 20$  mag, with individual galaxies assigned membership classifications based mainly on radial velocity and surface brightness measurements. The VCC also provides coordinates, integrated magnitudes, diameters, axial ratios, and morphological types for nearly all galaxies, and continues to be an important resource for Virgo Cluster studies even now, a quarter century after its publication.

However, although the VCC continues to have the important advantages of completeness and homogeneity, the photographic nature of the survey, the fact that it was carried out in a single bandpass, and its relatively modest angular resolution limited its ability to probe simultaneously the central and global properties of galaxies in a fully automated way.

An important advance in this area was made possible with the installation of Advanced Camera for Surveys (ACS) on the *Hubble Space Telescope (HST)* in 2002. The ACS Virgo Cluster Survey (ACSVCS) was a Cycle 11 *HST* program (GO-9401; Côté et al. 2004) that was designed to capitalize on both the excellent image quality of ACS ( $\text{FWHM} \approx 0'.1$ , which corresponds to a physical scale of  $\approx 8$  pc at a distance of 16.5 Mpc) and its relatively wide field of view ( $\approx 11 \text{ arcmin}^2$ , or roughly double that of WFPC2) to study, simultaneously, the core and global structure of early-type galaxies in the Virgo Cluster. For each of 100 early-type members of the Virgo Cluster,  $g$ - and  $z$ -band ACS/WFC images (F475W and F850LP, respectively) were obtained in a single *HST* orbit. The program galaxies spanned a 6.7 mag range in  $B_T$  from the VCC, with no restriction on morphological type aside from an “early-type” classification in Binggeli et al. (1985), i.e., E, E/S0, S0/E, S0, dS0, dS0,N, dE or dE,N. As shown in P. Côté et al. (2010, in preparation), this conservative selection on morphology effectively ensured that the ACSVCS targeted Virgo’s “red sequence” (e.g., Visvanathan & Sandage 1977; see, also, Strateva et al. 2001; Baldry et al. 2004 and Section 3.4 below) population with a high level of completeness (i.e., the sample is 100% complete for  $B_T \lesssim 12$  and  $\approx 60\%$  complete for early-type galaxies brighter than  $B_T = 16$ ).

In addition to being used in a comprehensive analysis of the core and global structure of early-type galaxies (see below), the ACSVCS imaging formed the basis of many related studies, including the connection between globular clusters (GCs) and low-mass X-ray binaries (Jordán et al. 2004; Sivakoff et al. 2007), the measurement and calibration of surface brightness fluctuations, magnitudes and distances (Mei et al. 2005a, 2005b, 2007), the connection between GCs and ultracompact dwarf galaxies (Haşegan et al. 2005), the color distribution of GCs (Peng et al. 2006a), the half-light radii of GCs and their use as a distance indicator (Jordán et al. 2005), diffuse star clusters in early-type galaxies (Peng et al. 2006b), and the luminosity function, color–magnitude relations (CMRs), and formation efficiencies of GCs in early-type galaxies (Jordán et al. 2006, 2007, 2009; Mieske et al. 2006; Peng et al. 2008).

The isophotal and structural analysis of the ACSVCS galaxies was presented in Ferrarese et al. (2006a), the first study to examine simultaneously the core and global structure of a large sample of nearby galaxies using *HST* imaging. In a departure from previous studies, which nearly always parameterized the inner structure of galaxies using a broken power-law, or “Nuker,” model, the surface brightness profiles of the ACSVCS galaxies were parameterized using the Sérsic family of models (e.g., Sérsic 1968; Graham & Guzmán 2003; Graham et al. 2003; Trujillo et al. 2004). These models were found to provide accurate representations of the surface brightness profiles on scales greater than a few percent of the effective radius. On smaller scales, the brightness profiles of bright ( $M_B \lesssim -20$ ) galaxies showed central *deficits* with respect to the inward extrapolation of the Sérsic models; fainter galaxies usually show central *excesses*, or, alternatively, central stellar nuclei (Graham et al. 2003; Côté et al. 2006, 2007, 2008; Ferrarese et al. 2006b).<sup>6</sup> Ferrarese et al. (2006a) also noted that, based on their fitted Sérsic parameters, the early-type “dwarf” population in Virgo appears to form a low-luminosity extension to the early-type “giant” population in terms of their photometric

and structural parameters (albeit with some evidence that the dwarfs formed a “complex and diverse population”). Several other studies have reached similar conclusions in recent years (e.g., Graham et al. 2003; Graham & Guzman 2003; Gavazzi et al. 2005; Misgeld et al. 2008, 2009; Janz & Lisker 2008, 2009; but see Kormendy et al. 2009 for a different view).

The implications of these findings are potentially profound, as they would suggest that successful models for small-scale structure formation should yield galaxies having photometric and structural properties that vary smoothly and systematically with luminosity/mass, rather than dividing neatly into two non-overlapping populations that originated through fundamentally distinct formation channels (i.e., a “dichotomy” between so-called dwarfs and giants; Kormendy 1985). Two sequences, apparently separating compact ellipticals and ultra-compact dwarf galaxies from “normal” dwarf galaxies, were identified by Dabringhausen et al. (2008), although they did not describe this divergence in terms of a “dichotomy” (see also Figure 10 of Haşegan et al. 2005). In any case, it is clearly important to check that the ACSVCS conclusions are robust to the choice of galaxy model, particularly since this sample has become the focus of a number of follow-up studies at X-ray to radio wavelengths (e.g., Gallo et al. 2008, 2010; Capetti et al. 2009).

In this paper, we perform such a check by carrying out aperture photometry on the ACSVCS sample, using standard curve-of-growth (COG) techniques that have been employed in many previous studies: e.g., Longo et al. (1983), Binggeli et al. (1984), Poulain (1988), Burstein et al. (1987), de Vaucouleurs (1977), de Vaucouleurs & Corwin (1977), de Vaucouleurs & Bollinger (1977), de Vaucouleurs et al. (1977, 1991), Buta et al. (1995), Prugniel & Simien (1997), Prugniel & Heraudeau (1998) and Janz & Lisker (2008, 2009). A secondary issue to consider is that the brightest and most extended galaxies in the ACSVCS have spatial extents that are sometimes larger than the  $200'' \times 200''$  ACS field of view. This required Ferrarese et al. (2006a) to combine the ACS surface brightness profiles with published (mainly photographic) profiles measured from the ground. To explore whether this field-of-view limitation (or the choice of Sérsic model as a parameterization) has any significant effect on the derived parameters for ACSVCS galaxies, we require wide-field CCD images that have been flat-fielded to a high level of precision. Although it will eventually be superseded by a very deep, multi-filter imaging survey of the Virgo Cluster that is now underway using the MegaCam instrument on the Canada-France-Hawaii Telescope (i.e., the Next Generation Virgo Cluster Survey (NGVS); L. Ferrarese et al. 2010, in preparation), the state-of-the-art wide-field CCD imaging database for this benchmark cluster is currently the Sloan Digital Sky Survey (SDSS). Indeed, several recent studies of the Virgo Cluster and its constituent galaxies have made use of this excellent resource (e.g., Lisker et al. 2007; Rines & Geller 2008; Janz & Lisker 2008, 2009; McDonald et al. 2009).

The structure of this data paper, which is intended to provide multi-band photometric and structural parameters for 100 ACSVCS galaxies, is as follows. In Section 2, we summarize the observational material used in this study and describe our data reduction pipeline. In Section 3, we present internal and external comparisons of our measurements with those from other studies, and examine the global properties of our program galaxies, including their photometric and structural scaling relations, intrinsic shapes, and CMRs. We conclude in Section 4 with a summary of our findings and outline some directions for future research.

<sup>6</sup> This finding has recently been confirmed by Kormendy et al. (2009) who re-analyzed the ACS imaging for a subset of the 100 ACSVCS galaxies.

## 2. DATA AND ANALYSIS

The data resource for our analysis is the SDSS Data Release 5 (DR5). The SDSS uses a 2.5 m  $f/5$  multi-filter imaging and spectroscopic telescope located at the Apache Point Observatory in New Mexico (York et al. 2000). The imaging of SDSS is carried out in a “time delay and integrate” mode using a camera consisting of thirty  $2048 \times 2048$  CCDs that collect data simultaneously in five bands ( $ugriz$ ) with an exposure time of  $\sim 55$  s per band (Gunn et al. 1998); these long SDSS scans are broken up into smaller  $13.5' \times 9'$  fields for photometric processing. In many cases, and particularly for bright galaxies that subtend large angles on the sky (i.e., effective diameters up to  $\approx 4'-8'$  at the distance of the Virgo Cluster), the large-format CCDs, and the accurate flat-fielding that is possible as a result of the drift-scan-like operating mode, are well suited to the measurement of surface photometry and aperture magnitudes, although this still requires careful stitching of neighboring runs and camera columns to produce flat and uniform images with matching skies (see West et al. 2010). As the  $\approx 10^4$  deg $^2$  SDSS survey region includes the Virgo Cluster in its entirety, the five-band imaging from this survey presents an excellent opportunity to determine non-parametric photometric and structural parameters for the complete sample of galaxies from the ACSVCS (i.e., for the bright “giants” and faint “dwarfs” alike).

The goal of our study is the measurement of model-independent photometric and structural parameters for the ACSVCS galaxies. The primary challenges in this regard come from galaxies at the upper end of the Virgo luminosity function, which can extend over spatial scales of many arcminutes (i.e., with effective radii in the range  $\approx 2'-4'$ ; e.g., Caon et al. 1990, 1994; Ferrarese et al. 2006a) and from galaxies in crowded, high-density regions of the cluster or otherwise with close companions. Indeed, the SDSS catalog data are not adequate for our analysis because of deblending and sky subtraction problems for the largest galaxies, which often extend across field boundaries (see West et al. 2010). We therefore used the SDSS fields and performed our own sky subtraction, field mosaicking, and photometric measurements, as discussed below.

The first issue to consider is the choice of bandpass for our analysis. Generally speaking, it is the  $gri$  images that have the best signal-to-noise values of the five SDSS bands, with the two bluer filters having the advantage of darker skies and, hence, somewhat more reliable estimates of the background levels. If we consider the specific case of VCC1422, an intermediate-luminosity galaxy (classified in the past alternately as E, E1,N:, E3,N:, dE or Sph,N; P. Côté et al. 2010, in preparation) that is in many ways representative of the sample, the total  $g$ -band counts within twice the Petrosian radius (see Section 2.2) are  $\approx 1030$  counts, and the ratio between total galaxy counts and the standard deviation in the sky is  $\sim 5.3 \times 10^4$ . The latter is slightly higher (by 6%–10%) than in the  $r$  or  $i$  bands (with the latter bandpass showing a higher and more variable sky). The ratios for the  $u$  and  $z$  band counts are much lower (by factors of 3.6 and 4.2, respectively) as a result of the intrinsically lower galaxy luminosity in the  $u$ -band, and the noisier sky in both bands (particularly in  $z$ , where the rms scatter is  $\sim 10\times$  that in  $g$ ). We therefore adopt  $g$  and  $r$  as the primary bandpasses for our analysis, with  $g$  having the added benefit that it allows a direct comparison to the results from the ACSVCS (which relied on F475W imaging).

### 2.1. Construction of SDSS Mosaics

It is well known that very extended galaxies, such as many of the bright galaxies in the Virgo Cluster, pose a challenge to the standard SDSS pipeline because of sky estimation problems and deblending errors (see, e.g., Blanton et al. 2005; West et al. 2010). In this section, we describe briefly the procedures used to create the final, smoothed SDSS mosaic images used in the measurement of the galaxy parameters. We refer the interested reader to West et al. (2010) where the methodology used to generate these wide-field SDSS mosaics is described in more detail.

All SDSS images, in all five bands, lying within a specified distance of each galaxy were first downloaded. The adopted field sizes were  $1^\circ \times 1^\circ$  for the five brightest galaxies (i.e., VCC1226, VCC1316, VCC1978, VCC881, and VCC798) with a plate scale of  $1''.188\text{ pixel}^{-1}$ ,  $30' \times 30'$  for the 6th to 20th-ranked galaxies (see Table 1), and  $10' \times 10'$  for all remaining galaxies. The plate scale for the latter two field sizes were both  $0''.792\text{ pixel}^{-1}$ , with the exception of three very compact galaxies (i.e., VCC1192, 1199, and 1297) for which a plate scale of  $0''.396\text{ pixel}^{-1}$  was used. Images were then joined together to form a master mosaic for each filter that was visually inspected to confirm that (1) the visible extent of each galaxy was comfortably contained within the adopted field and (2) bright stars and their artifacts were excluded.

Before the fields were mosaicked, each field was individually sky subtracted. To do so, SExtractor (Bertin & Arnouts 1996) was first run on the master  $r$ -band image to identify sources and mask non-sky pixels (e.g., background galaxies, foreground stars, bad pixels) generating a final mask image. A tilted plane was fitted to the remaining sky pixels and this fit was then subtracted from the mosaic, yielding a final image with zero sky and unmasked sources (e.g., galaxies and stars). The same procedure was repeated for the four remaining bands ( $ugiz$ ) using the masks derived from the  $r$ -band image. To verify the accuracy of the sky subtraction, West et al. (2010) used four different parameterizations for the shape of the background, ranging from first order (i.e., a tilted plane) to fourth order (i.e., a fourth-order polynomial in both  $x$  and  $y$ ) models. The precise choice of sky model was found to introduce an error of no more than  $\sim 0.01$  mag on the resulting photometry. Individual sky-subtracted fields were then mosaicked to create the final, smoothed SDSS mosaic images.

### 2.2. Source Masking

The next challenge is to minimize, or eliminate altogether, contamination from nearby sources when performing photometry on the sky-subtracted, mosaic images of the program galaxies. Of course, a large aperture is desirable because we wish to include as much light as possible for these extended objects. However, excessively large apertures will lead to an enhanced level of contamination from additional sources in the field. Thus, two pre-requisites for measuring parameters for the program galaxies are (1) masking of all field sources surrounding the target (i.e., Galactic field stars and other galaxies, whether they are Virgo members or not) and (2) determining a proper aperture size for the surface photometry.

We developed a customized masking routine that has a level of flexibility which is convenient for this task, given the diversity in properties of the possible contaminants. As a first step, the mean and standard deviation of the sky,  $\sigma_{\text{sky}}$ , is determined and the global shape of the galaxy is calculated by fitting its





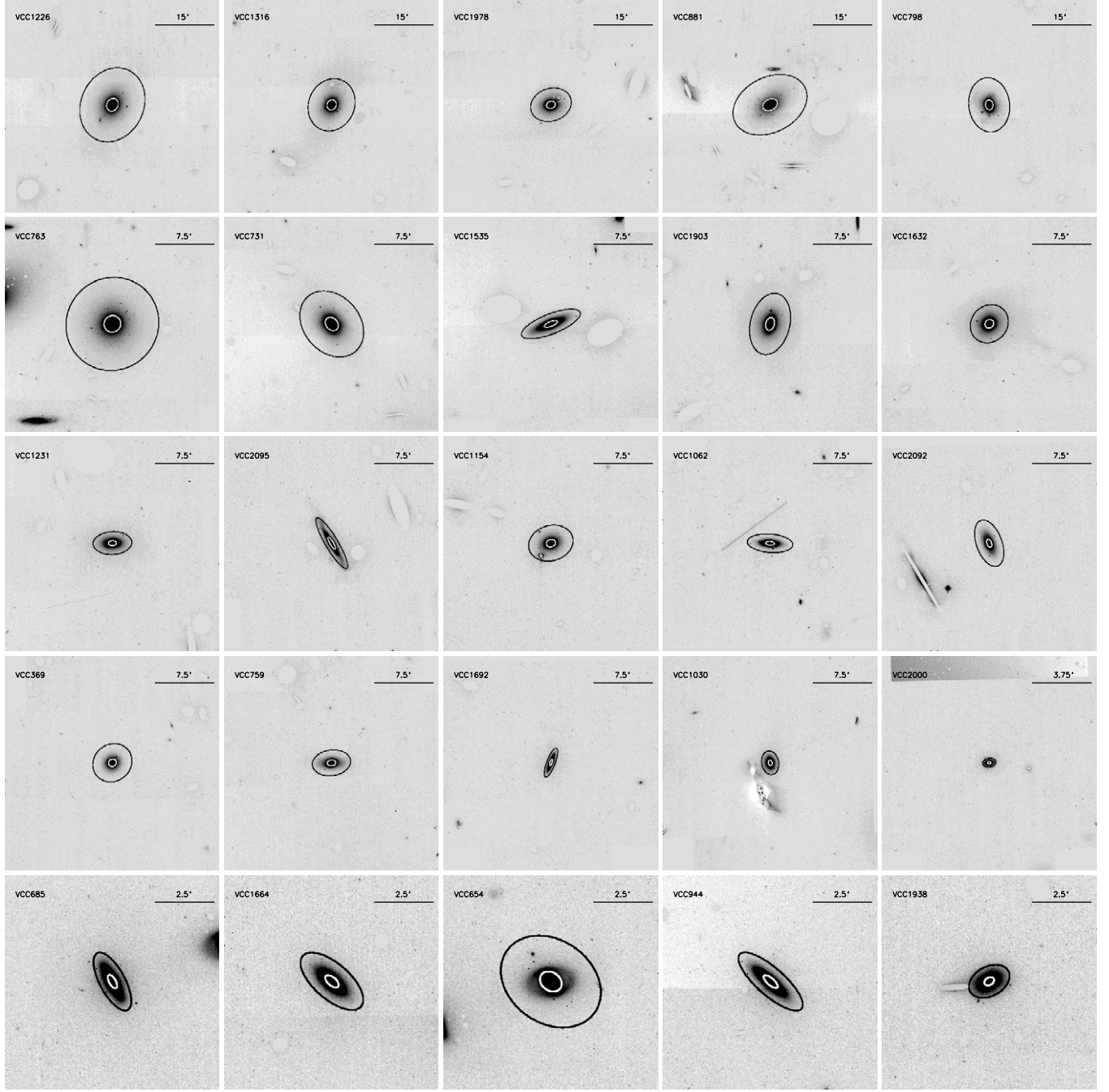


**Figure 1.** Masked  $g$ -band mosaics for the 100 ACSVCS galaxies ordered by  $B$ -band magnitude from Binggeli et al. (1985), with fainter galaxies appearing to the right and to the bottom. All images are background subtracted. The angular scale and VCC identification number are given in the upper right and left corners of each panel. The outer ellipse shows the aperture,  $A_R$ , for the photometry, while the inner ellipse shows the measured effective Petrosian radius,  $R_{50}$ . Note the horizontal bands in a few images are where different frames were joined. Although the sky level has been carefully removed, the sky noise may become obvious if the original sky level is high.

Assuming the sky is azimuthally symmetric around individual galaxies, we first defined concentric ellipses around each galaxy with shape and orientation identical to that measured at the  $5\sigma_{\text{sky}}$  isophote. To mask out field sources, we replaced them with the median values of the concentric ellipses passing through the sources, with the masked regions being the elliptical areas within the  $3\sigma_{\text{sky}}$  isophote of each source. The advantage of taking the azimuthally averaged value is to avoid overestimates of the sky background near saturated or unusually extended sources. Because we did not wish to influence the photometry close to the

galaxy center, we masked only those sources outside the  $5\sigma_{\text{sky}}$  isophote.<sup>8</sup> In a few cases, the galaxy was found to have a bright source nearby: e.g., VCC1978 (M59) has a 12th magnitude spiral galaxy (VCC1972 = NGC4647) projected  $2.57'$  to the northwest. In such cases, GALFIT (Peng et al. 2002) was used to model and subtract the companion galaxies, usually with a single Sérsic model. The photometric error caused by the removal process depends on the angular separation between the

<sup>8</sup> Again using VCC1422 as an example, this corresponds to  $\approx 21''$ .

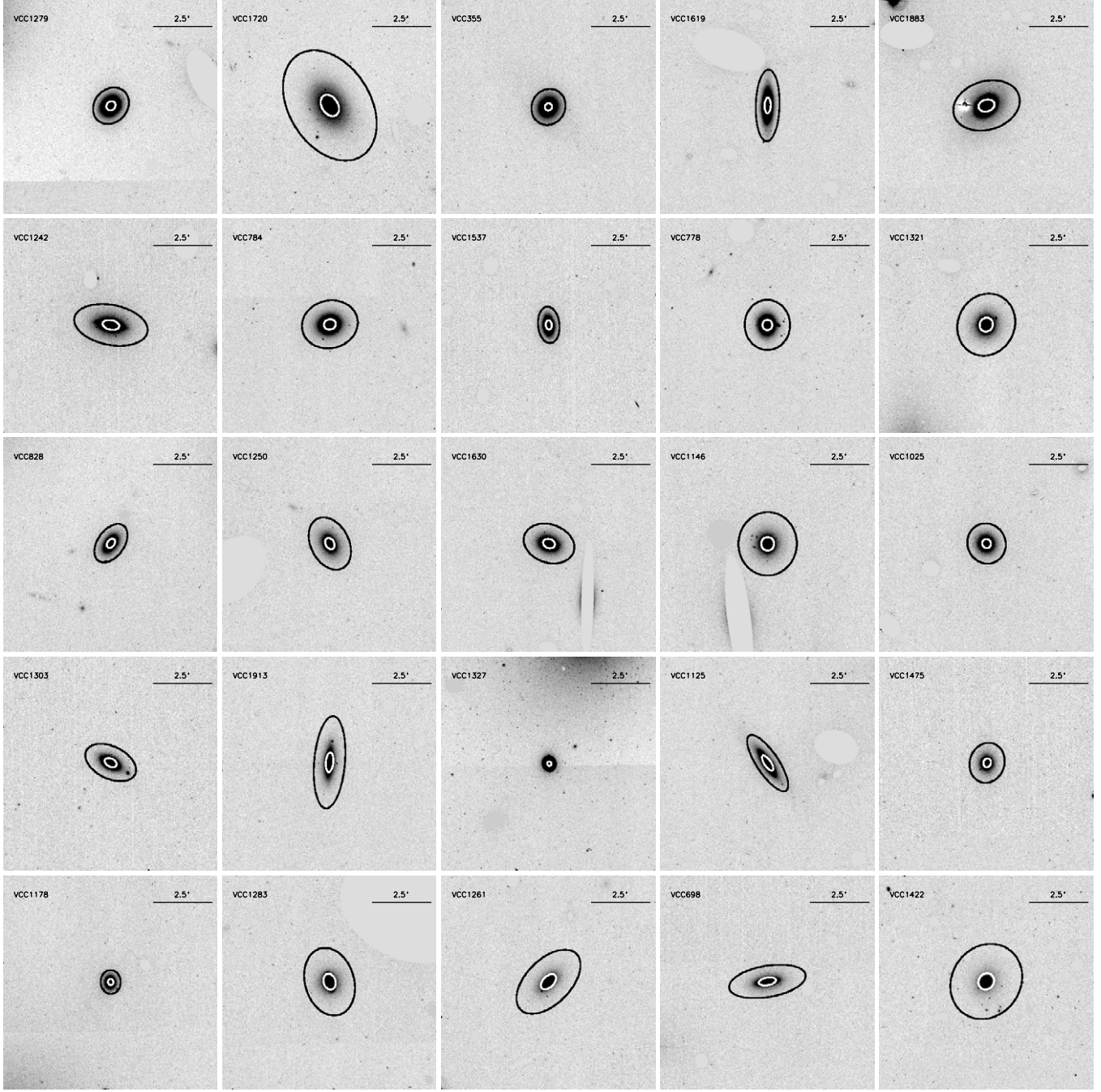


Figure 1. (Continued)

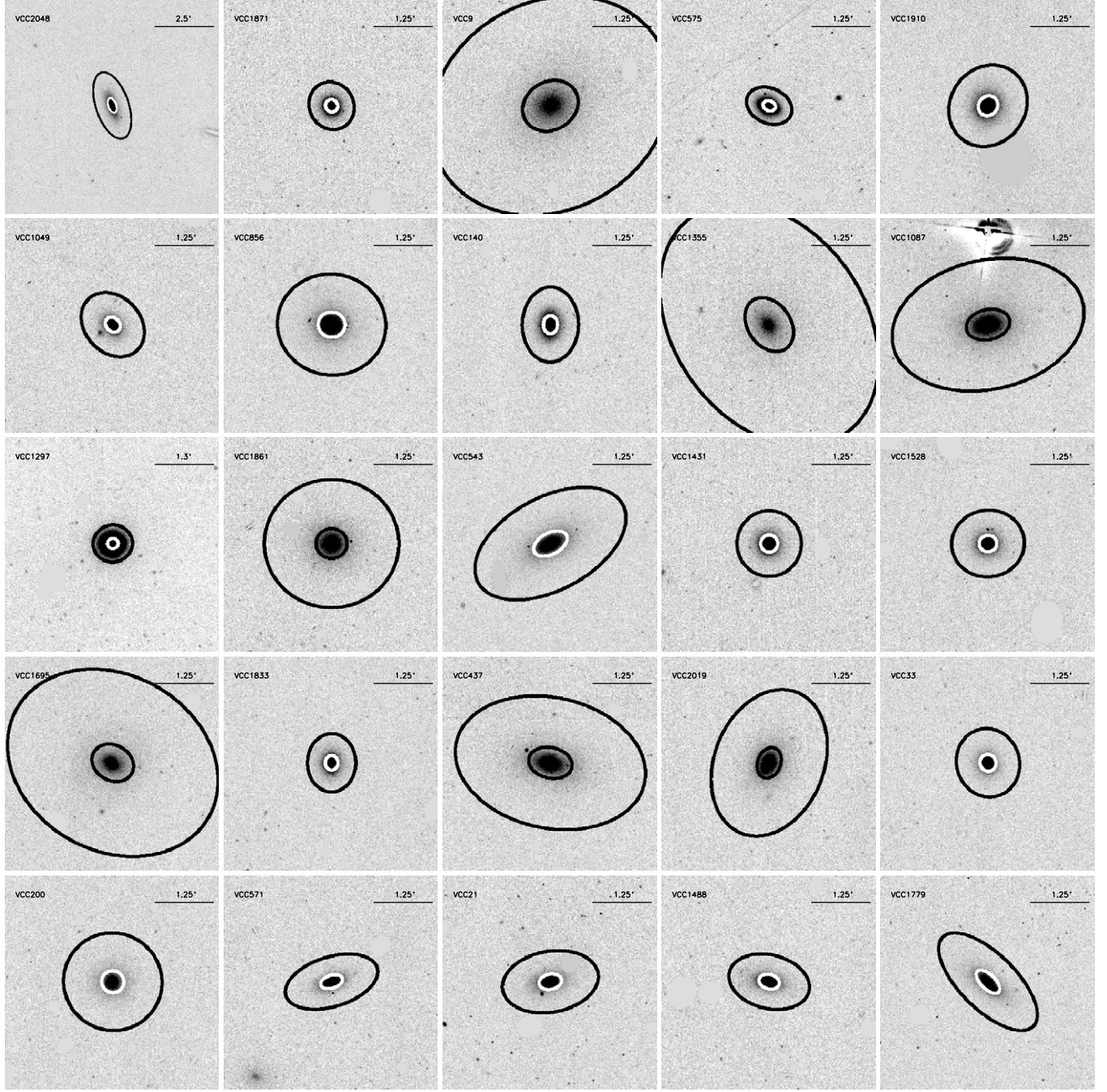
central galaxy and field source; typically, the error is less than 1% per pixel for the target galaxy.

Figure 1 shows masked  $g$ -band mosaic images for all 100 galaxies. The angular scale and galaxy identification number from the VCC are given in the upper right and upper left corners. The outer ellipse shows the aperture used for the photometric analysis (see Section 2.3) while the inner ellipse is drawn at the measured effective Petrosian radius of the galaxy,  $R_{50} = \sqrt{a_{50}b_{50}}$ , where  $a_{50}$  and  $b_{50}$  are the effective Petrosian semi-major and semi-minor axes, respectively (see Section 2.3.2). Note that while it is sometimes possible to see residuals from the masking process, for the most part, these residuals fall outside of the aperture. Figure 2 shows the initial and masked  $g$ -band images for five representative galaxies from the ACSVCS;

these are the 1st, 25th, 50th, 75th, and 100th ranked galaxies in the sample in terms of their apparent  $B$ -band magnitude from the VCC (Binggeli et al. 1985). COG profiles for these same galaxies, which show the enclosed  $g$ -band magnitude as a function of aperture radius, are given in Figure 3.

### 2.3. Measurement of Photometric and Structural Parameters

The masked, background-subtracted  $g$ -band mosaic images described above form the basis of our parametric and non-parametric analyses. We focus first on the parametric results and turn our attention to the model-independent, COG analysis in Section 2.3.2.



**Figure 1.** (Continued)

### 2.3.1. Parametric Approach: Sérsic Model Fits

The masked, background-subtracted images were used to derive  $ugriz$  surface brightness profiles for all 100 galaxies using the IRAF<sup>9</sup> task ELLIPSE (Jedrzejewski 1987).

For the majority of galaxies, the control parameters were unconstrained when running ELLIPSE on each of the  $ugriz$  images, i.e., the center, ellipticity, and position angle were allowed to vary independently. The initial guess of the isophote center was determined by the position of the peak for a  $10 \times 10$  pixel box (corresponding to  $8'' \times 8''$  for all but the brightest five

galaxies) centered on a visual estimate of the galaxy photocenter. For some faint galaxies (e.g., VCC1512, VCC1489, VCC1661), the isophote centers were later fixed to the  $g$ -band values for images with a relatively lower signal-to-noise ratio (S/N; typically the  $u$  and  $z$  band data). To minimize the effects of bright, small-scale features (e.g., GCs, foreground stars, or bad pixels), we applied  $\sigma$  clipping on pixels deviating by more than three times of the standard deviation of the mean intensity in each isophote.

Consistent with the approach adopted in several recent studies (e.g., Graham & Guzmán 2003; Erwin et al. 2005; Ferrarese et al. 2006a, 2006b; Côté 2006, 2007; Saviane & Jerjen 2007; Gallo et al. 2008), we then fitted the azimuthally averaged surface brightness profiles of our program galaxies with Sérsic (1968)

<sup>9</sup> IRAF is distributed by the National Optical Astronomy Observatory, which is operated by the Association of Universities for Research in Astronomy, Inc., under cooperative agreement with the National Science Foundation.

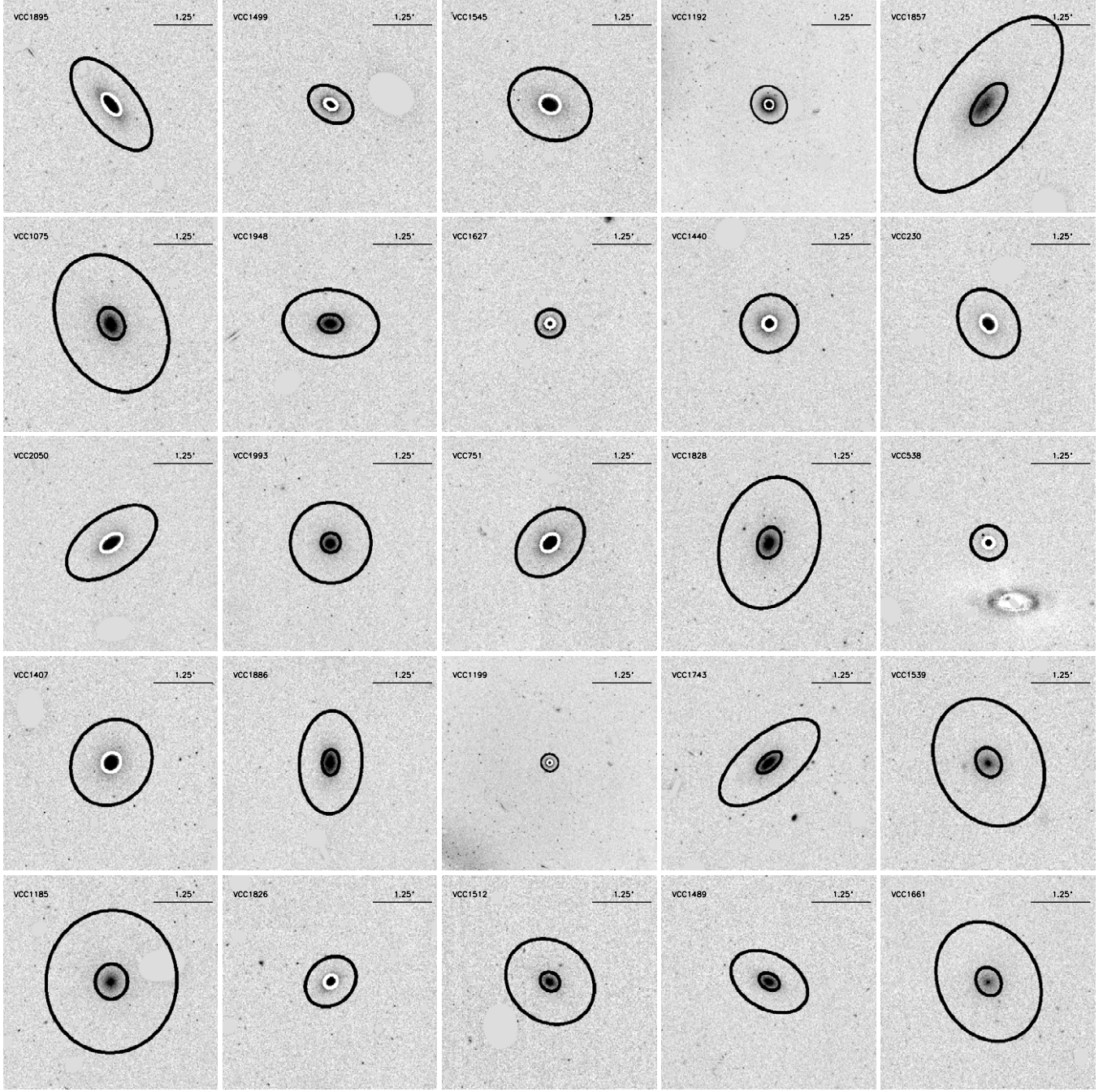


Figure 1. (Continued)

models,

$$I(r) = I_e \exp\{-b_n[(R/R_e)^{1/n_s} - 1]\}, \quad (1)$$

where  $I_e$  is the intensity at the effective radius,  $n_s$  is an index that measures the overall galaxy concentration (i.e., profile curvature),  $R_e$  is the effective radius, and  $b_n \simeq 1.9992n_s - 0.3271$  (Capaccioli 1989; Prugniel & Simien 1997; Ciotti & Bertin 1999). Note that a Sérsic model becomes an exponential law when  $n_s = 1$ , which often provides a good match to the surface brightness profiles of dwarf galaxies (see, e.g., Ferguson & Binggeli 1994; Mateo 1998). When  $n_s = 4$ , Equation (1) takes the form of a classical de Vaucouleurs (1948) law, which is a reasonable fit to the surface brightness profiles of many bright elliptical galaxies, although it has been recognized for some time that there are luminosity-dependent departures

from this particular law (e.g., Michard 1985; Capaccioli 1987; Schombert 1986; Binggeli & Cameron 1991; Prugniel et al. 1992; Capaccioli et al. 1992).

In practice, for galaxies brighter than  $B_T = 11$  or  $M_B \approx -20.2$  (Côté et al. 2004; Mei et al. 2007), we limited the fit to regions outside the “break radius,”  $R_b$ , where there are clear inner departures from Sérsic laws (in the sense that the models overpredict the central surface brightness; see, e.g., Graham & Guzmán 2003; Graham et al. 2003; Ferrarese et al. 2006a, 2006b; Côté et al. 2006, 2007). For galaxies fainter than  $B_T = 11$ , which usually show a surface brightness excess due to the presence of a central nuclear component that lies above the inward extrapolation of the fitted Sérsic model (Côté et al. 2006, 2007), we excluded the central  $R = 2''$ . (Note that the typical seeing disk in SDSS is FWHM =  $1.3''$ – $1.6''$ ; York

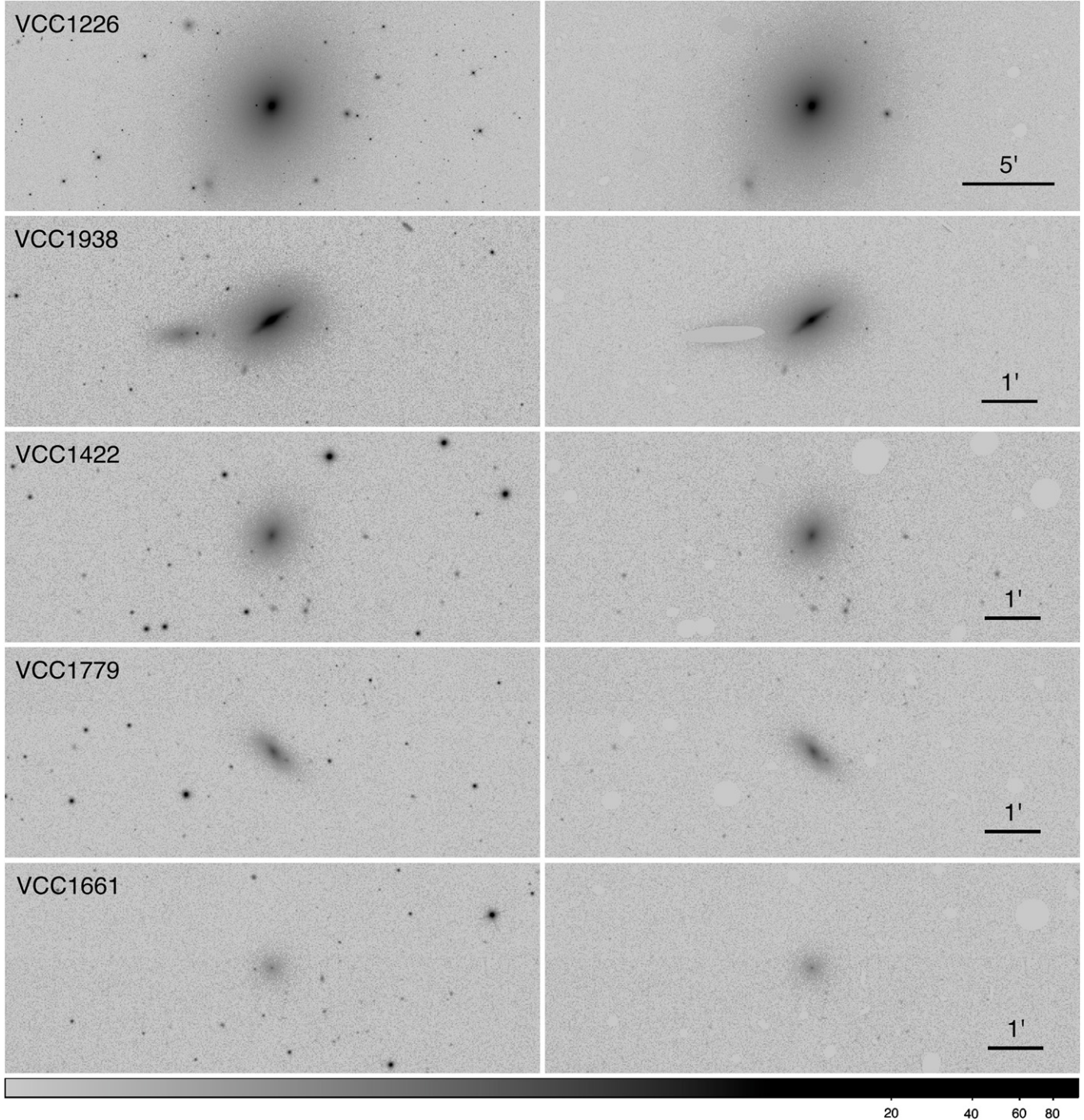


**Figure 2.** First row: raw (left) and masked (right)  $g$ -band mosaic images for VCC1226, the first-ranked member of the Virgo Cluster and the brightest galaxy in the ACSVCS. Second row: raw and masked images for VCC1938, the 25th-ranked galaxy. Third row: raw and masked images for VCC1422, the 50th-ranked galaxy. Fourth row: raw and masked images for VCC1779, the 75th-ranked galaxy. Fifth row: raw and masked images for VCC1661, the faintest galaxy in the ACSVCS.

et al. 2000). A Levenberg–Marquardt minimization technique was used to determine the best-fit Sérsic model parameters outside these central regions, assigning equal weight to all points in the SDSS surface brightness profiles. Finally, the five-band surface brightness profiles and fitted Sérsic models were used to derive mean colors for the galaxies in three different radial regions, from (1)  $1'' < R < 10''$ ; (2)  $1'' < R < R_e$ ; and (3)  $R = 0$  to infinity, a “global” mean color based on the total magnitudes deduced from the fitted models.

Figure 4 presents surface brightness and color profiles for the five representative galaxies shown in Figures 2 and 3, plotted

down to a level of 3% of the sky brightness. In the left panels, the dash blue curve shows the Sérsic model fitted to the  $g$ -band profile beyond the central  $2''$ . For comparison, the gray points show the  $g$ -band profiles derived from the ACSVCS (Ferrarese et al. 2006a; L. Ferrarese et al. 2010, in preparation), along with the ACSVCS fitted model (i.e., omitting the central, nuclear component, which appears as an upward inflection in the profile on scales of a few tenths of an arcsecond). Note that for VCC1226 (M49), the ACS profile was extended by matching to published ground-based surface photometry, as was the case for all the brightest galaxies (see Section 3.2 of Ferrarese et al.

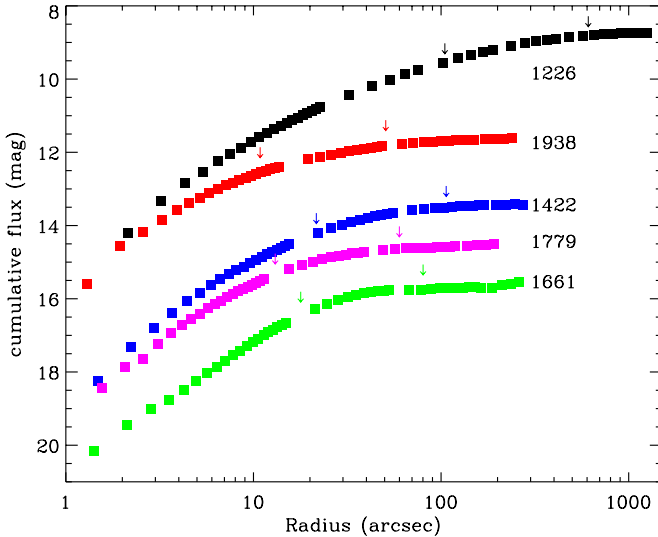


**Figure 3.** Curve-of-growth results for the five representative galaxies from the preceding figure, showing enclosed  $g$ -band magnitude as a function of aperture radius. For each galaxy, the two arrows show the effective Petrosian radius,  $R_{50}$ , and aperture radius,  $A_r$ , taken to be twice the Petrosian radius. See Section 2.3.2 for details.

(A color version of this figure is available in the online journal.)

2006b). The gray curve shown for this galaxy in Figure 4 is a “core-Sérsic” model (Graham et al. 2003; Trujillo et al. 2004), in which the outer Sérsic law transitions to a power-law profile inside a “break radius” of  $R_b \sim 2''$ . For the remaining galaxies, it can be seen that the SDSS profiles in  $gri$  typically extend beyond those from the ACSVCS by  $\approx 10'' - 25''$  ( $\approx 20\% - 40\%$  in radius), although in the regions of overlap the S/N is significantly lower. This figure further illustrates that the SDSS imaging—while well suited to an examination of the *global structure* of the program galaxies—is no substitute for the *HST* data for probing the structure in the galaxy cores.

### 2.3.2. Nonparametric Approach: Curve-of-growth/Petrosian Photometry

In this section, we describe the procedures used to perform a COG analysis using the  $g$ -band images in order to determine a total magnitude, effective radius, and mean effective surface brightness for each galaxy. This procedure requires the adoption of an optimum elliptical aperture within which we compute the cumulative flux profile. Ideally, the aperture size should be large enough to contain most or all of the flux for a galaxy, but small enough to ensure that the cumulative sky noise is small compared to the galaxy signal.

The Petrosian ratio  $Q_p$  for a galaxy (Petrosian 1976; Blanton et al. 2001) is defined as

$$Q_p(R) = \frac{\int_{0.8R}^{1.25R} dR' 2\pi R' I(R') / (\pi [1.25^2 - 0.8^2] R^2)}{\int_0^R dR' 2\pi r' I(R') / (\pi R^2)}, \quad (2)$$

where  $I(R)$  is the azimuthally averaged surface brightness profile. We used elliptical apertures in the analysis with aspect ratio and orientation angle defined by the  $5\sigma_{\text{sky}}$  isophote of the galaxy (Section 2.2).  $R$  denotes the geometric mean radius ( $R = \sqrt{ab}$ ) of the elliptical aperture. We remind the reader that the radial scales discussed here and afterward refer to the geometric mean radii derived from elliptical, rather than circular,

photometry. The Petrosian radius,  $R_p$ , is then defined as the radius at which  $Q_p(R_p)$  equals 0.2 (Blanton et al. 2001) so that the Petrosian flux,  $F_p$ , in any band is defined as the flux within  $2R_p$ :

$$F_p = \int_0^{2R_p} 2\pi R' I(R') dR', \quad (3)$$

$F_p$  should recover essentially all of the flux for a galaxy with an exponential brightness profile and about 80% of the flux for a de Vaucouleurs profile (see York et al. 2000). With  $F_p$  known, we can derive both the galaxy’s effective Petrosian radius,  $R_{50}$ , from  $a_{50}$  and  $b_{50}$  (see Section 2.2) and its average surface brightness within the effective Petrosian radius,  $\langle\mu\rangle_e \equiv g - A_g + 2.5 \log(2\pi R_{50}^2)$ . Note that  $R_{50}$  is defined here as the geometric mean radius of the galaxy containing half of the Petrosian flux, as is customary. Figure 3 shows the cumulative flux profile, plotted as a function of geometric mean radius for the same five representative galaxies shown in Figures 2. The inner and outer arrows on each profile show  $R_{50}$  and the aperture radius  $A_R \equiv 2R_p$ . Although the images used for the photometry is carefully processed (i.e., before the individual frames were mosaicked, the sky background is subtracted, and background sources masked), small errors in the background subtraction, or residuals from imperfect masking of interlopers, can still lead to deviations from the true asymptotic magnitude: e.g., note the slight rise in the outermost profiles for VCC1779 and VCC1661 in this figure. Fortunately, given the smaller values of  $A_r$  (e.g.,  $2R_p = 57''$  and  $76''$  for these galaxies) such fluctuations do not affect the derived parameters.

Strictly speaking, these nonparametric estimates of the total galaxy magnitude still require a correction to account for the “missing” light falling beyond the outermost aperture. This is true of any COG analysis (see, e.g., Burstein et al. 1987 and references therein). In principle, one could simply increase the aperture without applying any model correction. However, the extent to which the aperture size should be increased is rather subjective because it is again a tradeoff between signal from the galaxy, and noise from the sky and/or the field sources which are not perfectly masked. We therefore used Equations (5) and (6) of Graham et al. (2005) to convert magnitudes from the Petrosian to Sérsic system according to the concentration,  $c \equiv r_{90}/r_{50}$ , where  $r_{90}$  is the geometric mean radius of the galaxy containing 90% of the Petrosian flux (see also Janz & Lisker 2008, 2009). Note that galaxies with higher values of  $c$  are less centrally concentrated because they have relatively more light at larger radius. For our sample galaxies, the average size of the corrections is a fairly modest  $(\Delta g, \Delta R_e/R_{50}) = (0.08 \text{ mag}, 10\%)$  with a full range of  $(\Delta g, \Delta R_e/R_{50}) = (0.00 \text{ mag}, 0\%)$  at  $n_S < 1$  ( $g \lesssim 16.3$  mag) to  $(\Delta g, \Delta R_e/R_{50}) \approx (0.3 \text{ mag}, 70\%)$  for the six galaxies with concentration in the range  $n_S \sim 6-8$  ( $g \lesssim 10.0$  mag; see also Section 3.1).

### 2.3.3. Error Estimates for Curve-of-growth and Sérsic Parameters

Because the analysis described above was carried out independently in the  $g$  and  $r$  filters—the two bandpasses that have the highest quality imaging and the best-determined background levels—this gives us the opportunity to estimate typical uncertainties for the fitted parameters. Figure 5 shows the residuals between these different measurements, for both the COG results ( $b/a$ ,  $g$ ,  $\log R_e$ ,  $\langle\mu\rangle_e$ , and  $c$ ) and those obtained by fitting Sérsic models ( $\log n_s$ ,  $g_s$ ,  $\log R_{e,S}$ , and  $\langle\mu\rangle_{e,S}$ ). In all cases, the residuals are in the sense of the  $g$ -band measurements minus those in the  $r$  band: i.e.,  $\Delta(b/a) \equiv (b/a)_g - (b/a)_r$ . The red

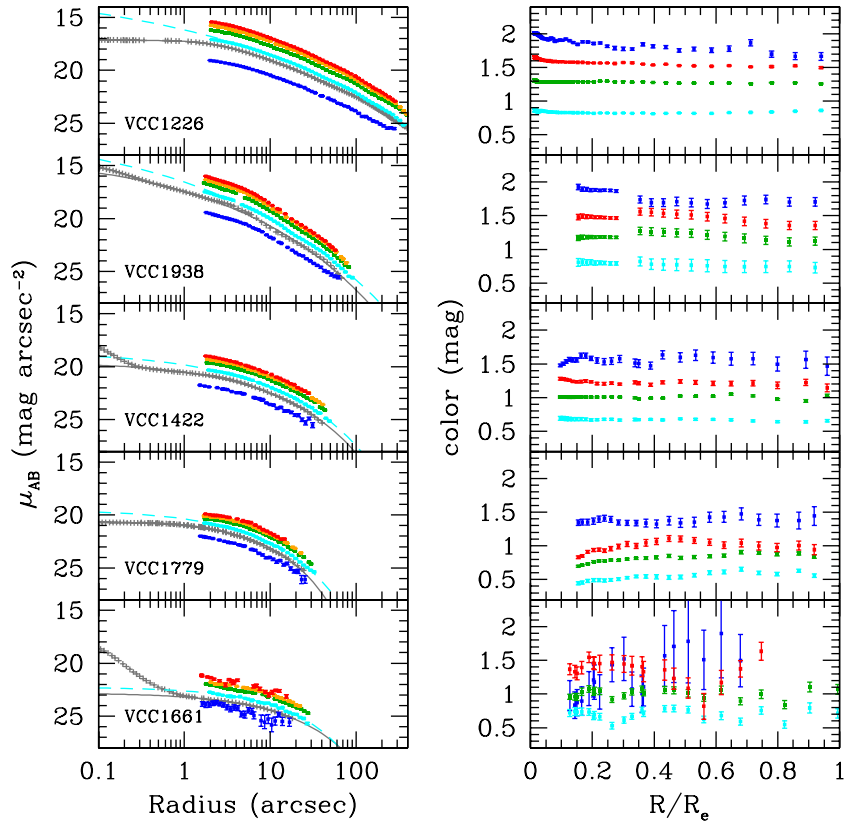


**Figure 4.** Left: SDSS surface brightness profiles for the five galaxies in Figures 2 and 3 along with the *HST*  $g$ -band profiles from the ACSVCS (Ferrarese et al. 2006a; L. Ferrarese et al. 2010, in preparation). SDSS profiles in  $ugriz$  are shown in blue, cyan, green, orange, and red, respectively, while those from the ACSVCS are shown in gray. The dashed blue curve in each panel shows our best-fit Sérsic model for the region outside of  $R = 2''$ . The smooth gray curve shows the Sérsic model fit to the outer (galaxy) component from the ACSVCS, neglecting the central light excesses (nuclei) which are often undetected in the SDSS profiles (see VCC1422). Note that both the ACSVCS profiles and models have been shifted downward by 0.5 mag for clarity. Right: color profiles for these same galaxies plotted as a fraction of the effective radii. Results are shown for the  $u-g$  (blue),  $g-r$  (cyan),  $g-i$  (green), and  $g-z$  (red) color indices.

(A color version of this figure is available in the online journal.)

histogram in each panel shows the residuals, along with the normal distribution (blue curve) that has the appropriate standard deviation,  $\sigma_{\text{tot}}$ . The value of  $\sigma_{\text{tot}}$  is reported, along with the mean residual, above each panel. If we assume that the errors in the two bandpasses are equal, which seems reasonable given the similar quality of the  $gr$  imaging and the precision of the respective background determinations, then  $\sigma_{\text{tot}}^2 = \sigma_g^2 + \sigma_r^2$  and  $\sigma_g \simeq \sigma_r / \sqrt{2}$ . Thus, the typical uncertainties on our derived parameters are  $\sigma \approx 0.025$ –0.030 for  $b/a$ ,  $\log R_e$ , and  $\log R_{e,S}$ ;  $\sigma \approx 0.08$  for  $g$ ,  $c$ , and  $g_S$ ; and  $\sigma \approx 0.13$  for  $\langle \mu \rangle_e$  and  $\langle \mu \rangle_{e,S}$ . Of course, these values should probably be viewed as lower limits, since some possible sources of systematic error (such as the choices of inner and outer fit radii, weighting scheme, and minimum threshold above the sky used in the fitting) cannot be included in any simple way. Nevertheless, our aim is to provide an estimate of the mean error for each parameter to help guide the comparison of our results to those of previous researchers. Such comparisons, particularly to the results of Janz & Lisker (2009) who performed an entirely independent analysis of the SDSS data, show that the above estimates are unlikely to be underestimated by more than  $\sim 50\%$ .

### 3. RESULTS

The observed and derived parameters for our galaxies are presented in Tables 1–3. In the first six columns of Table 1, we report, from left to right, the galaxy identification numbers from

the ACSVCS and VCC, alternate names, adopted aperture size, axial ratio, and position angle (with both of these latter quantities measured by ellipse fitting at the  $5\sigma_{\text{sky}}$  isophote). Columns 7–9 give the “uncorrected” COG magnitude, effective radius, and mean effective surface brightness; aperture-corrected values for these same three parameters are given in Columns 10–12. The final three columns of this table give  $R_{90}$ , the concentration index,  $c$ , and a rough indication of the morphological type from P. Côté et al. (2010, in preparation); entries with a colon(:) indicate galaxies for which there are significant discrepancies amongst the classifiers over the correct type (see Section 3.2 for details). Some notes on the properties of individual galaxies are given in the final column of Table 1.

The results of the parametric modeling (Section 2.3.1) are presented in Table 2. From left to right, this table records the VCC identification number, effective surface brightness,  $\mu_e$ , Sérsic index,  $n_S$ , effective radius,  $R_{e,S}$ , total magnitude,  $g_S$ , and mean effective surface brightness,  $\langle \mu \rangle_e$ . As discussed above, all entries in Tables 1 and 2 refer to measurements made in the  $g$  band.

Table 3 summarizes our color measurements for these galaxies. The reported errors on the colors were determined by adding in quadrature the errors from Poisson noise in each band to the zero-point errors of 1.35% in  $u$  and  $z$  and 0.9% in  $gri$ .<sup>10</sup> From left to right, the columns in this table give the VCC identifica-

<sup>10</sup> See <http://www.sdss.org/dr5/algorithms/fluxcal.html>.

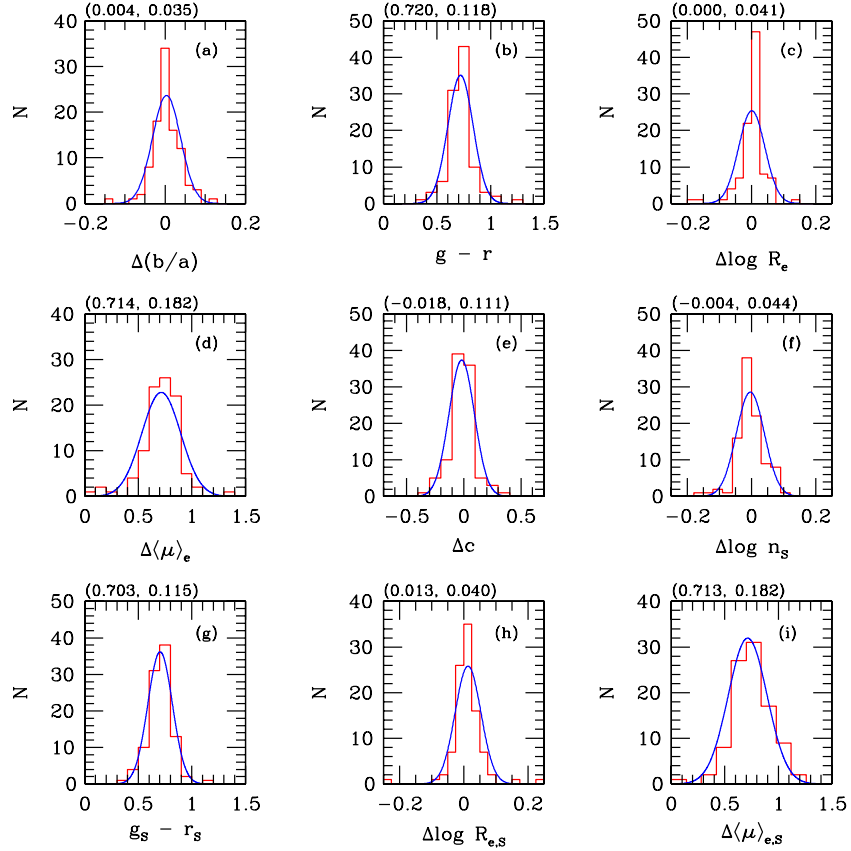


**Figure 5.** Red histograms show residuals between COG (panels (a–e)) and the best-fit Sérsic model parameters (panels (f–i)). All residuals refer to the  $g$ -band values minus those measured in the  $r$  band. The blue curve in each panel shows the fitted normal distribution. The mean residual and standard deviation for each parameter is labeled above each panel. Note that panels (b) and (g) refer to the galaxy colors, which follow a relation with magnitude and thus have an intrinsic scatter. (A color version of this figure is available in the online journal.)

tion number, and  $(u - g)$ ,  $(g - r)$ ,  $(g - i)$ , and  $(g - z)$  colors measured in three different ranges (see Section 2.3.1). In the next section, we compare our results to those found in previous investigations that used different observational material and analysis techniques.

### 3.1. Comparison to Previous Results

The most obvious comparison is with the ACSVCS itself as our sample galaxies have been taken directly from that survey (i.e., Table 1 of Côté et al. 2004). Figure 6 compares the parameters (i.e., total  $g$ -band magnitudes, Sérsic indices, effective radii, and mean effective  $g$ -band surface brightnesses) derived from our Sérsic model fits to those from the ACSVCS (Ferrarese et al. 2006a; L. Ferrarese et al. 2010, in preparation). The thin solid line in each panel shows the one-to-one relation while the dashed lines show least-squares fits:

$$\begin{aligned} g_{\text{vcs}} &= (1.006 \pm 0.012)g_s \\ &\quad + (0.04 \pm 0.16) \quad \sigma = 0.19 \\ \log n_{\text{vcs}} &= (0.816 \pm 0.061) \log n_s \\ &\quad + (0.04 \pm 0.03) \quad \sigma = 0.12 \\ \log R_{e,\text{vcs}} &= (0.986 \pm 0.030) \log R_{e,s} \\ &\quad - (0.02 \pm 0.04) \quad \sigma = 0.10 \\ \langle\mu\rangle_{e,\text{vcs}} &= (0.971 \pm 0.031)\langle\mu\rangle_{e,s} \\ &\quad + (0.55 \pm 0.64) \quad \sigma = 0.35. \end{aligned} \quad (4)$$

(In this figure, and in similar ones that follow it (e.g., Figures 8–10), the residuals between the two different measurements are shown in at the bottom of each panel, along with the least-squares fit (dashed line).) In general, there is very good agreement between the measured parameters from the two studies, aside from a small number of outliers (see Table 1 for notes on individual galaxies). Although the scatter is largest in panel (b), this scatter in  $n_s$  does not necessarily translate into equally large errors in the global parameters, where the effective radius, effective surface brightness, and total magnitudes are usually well determined. Of course, there are a few galaxies that are significant outliers in multiple panels, one of which is VCC1327. Note, however, that the SDSS results for this galaxy are unreliable because of the presence of a  $V \approx 11.7$  mag star located just  $2''.5$  to the southwest of the galaxy center. Likewise, VCC369 is a particularly challenging galaxy for a single-component model since its shape varies from round in the center ( $R \lesssim 6''$ ) and in the outskirts ( $R \gtrsim 50''$ ), to rather elongated at intermediate radii—probably due to the presence of a stellar bar (Ferrarese et al. 2006a). VCC2095 is the most extreme S0 galaxy in the ACSVCS sample, with a clear disk-like structure that is being viewed nearly edge on.

Before proceeding, we pause to compare the Sérsic indices measured from fitting the one-dimensional surface brightness profiles (i.e., the indices shown in Figure 6(b)) to the non-parametric concentration indices,  $c \equiv R_{90}/R_{50}$ , derived from the COG analysis. These different concentration measurements are plotted as a function of total (Sérsic)  $g$ -band magnitude in panels (a) and (b) of Figure 7. As expected, both indices







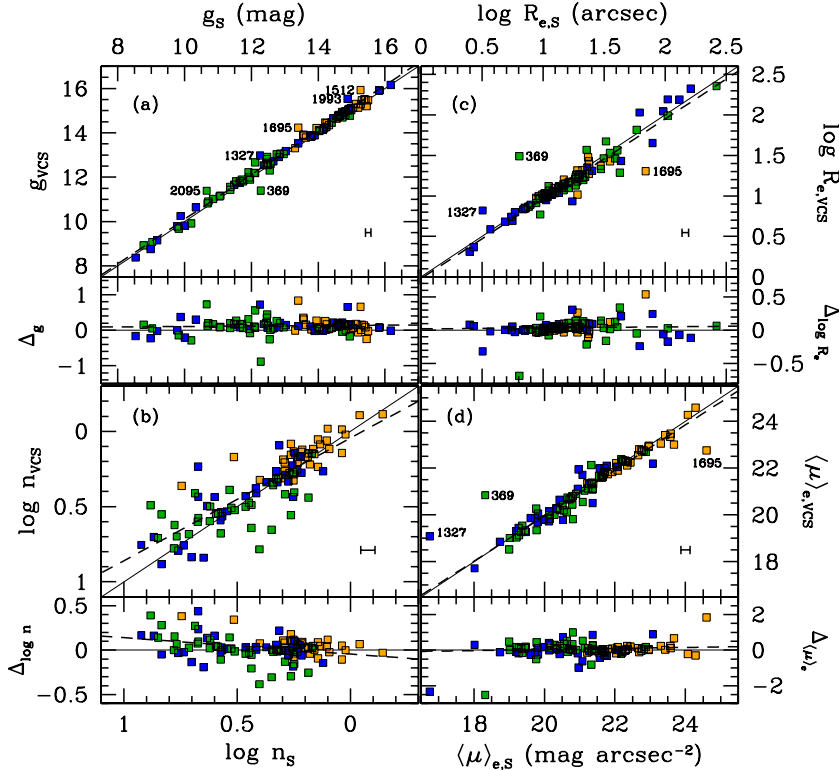


**Figure 6.** Comparison of our fitted Sérsic model parameters from the SDSS to those from the ACSVCS (Ferrarese et al. 2006a; L. Ferrarese et al. 2010, in preparation). Here, and in the figures that follow, galaxies have been crudely divided into three broad groups using the “consensus morphologies” tabulated in Table 1 (see the text for details) with elliptical (E), lenticular (S0), and dwarf (D) galaxies shown respectively by the blue, green and orange symbols; similarly, here, and Figures 8–10, the residuals between the two different measurements are shown in at the bottom of each panel, along with the least-squares fit (dashed line). The error bars in each panel show representative uncertainties. The thin solid line in each panel shows the one-to-one relation, while the dashed line gives the least-squares best-fit relation. Apart from a few outliers, there is good agreement between the two sets of measurements.

$$+ (0.44 \pm 0.38) \quad \sigma = 0.18,$$

where we have added a comparison of the mean axial ratios found in the two studies which, in the case of the Janz & Lisker (2009) analysis, was measured at the half-light semi-major axis (recall that our measurement was performed at the  $5\sigma_{\text{sky}}$  isophote). In any case, the agreement between the derived parameters is excellent. Although the same observational material is used in both studies, this comparison nevertheless demonstrates there are no systematic differences introduced by the different analysis techniques.

In panels (b)–(d) of Figure 9, we compare the corrected, COG measurements from this study to those from the ACSVCS, which are based on Sérsic-model fits to the surface brightness profiles (i.e., total magnitude, effective radius, and mean effective surface brightness). For completeness, panel (a) compares our  $g$ -band magnitudes to the photographic  $B$ -band measurements of Binggeli et al. (1985). These VCC magnitudes were derived from a comparison to photometric “standard” galaxies obtained from photoelectric aperture photometry for 109 galaxies, as described in Binggeli et al. (1984). The dashed line in each panel gives the least-squares relation:

$$\begin{aligned} B_{\text{vcc}} &= (0.901 \pm 0.018)g \\ &\quad + (1.65 \pm 0.23) \quad \sigma = 0.23 \\ g_{\text{vcs}} &= (1.021 \pm 0.015)g \\ &\quad - (0.18 \pm 0.19) \quad \sigma = 0.19 \\ \log R_{e,\text{vcs}} &= (1.080 \pm 0.047) \log R_e \\ &\quad - (0.12 \pm 0.06) \quad \sigma = 0.11 \end{aligned} \quad (6)$$

$$\begin{aligned} \langle\mu\rangle_{e,\text{vcs}} &= (0.996 \pm 0.044)\langle\mu\rangle_e \\ &\quad + (0.05 \pm 0.92) \quad \sigma = 0.40. \end{aligned}$$

The comparison in panel (a) reveals the mean random error for the widely used VCC magnitudes to be  $\approx 0.2$  mag, consistent with the findings of Binggeli & Cameron (1993; see also Gavazzi et al. 2005). Dividing the sample into three magnitude bins, we estimate the random errors in the VCC to be  $\approx 0.13$  mag for galaxies brighter than  $B_T = 12$ ,  $\approx 0.18$  mag for galaxies with  $12 \lesssim B_T \lesssim 14$ , and  $\approx 0.27$  mag for galaxies with  $14 \lesssim B_T \lesssim 16$ . As for the parametric results from the ACSVCS, there is overall excellent agreement between the COG parameters measured from the SDSS imaging. Perhaps surprisingly, this conclusion applies to all morphological groups, including the subset of galaxies classified as lenticulars. For instance, the rms scatter about the fitted linear relations in panels (a)–(d) is 0.21, 0.22, 0.13, and 0.49 for the S0s; these values differ only slightly from the respective values for the Es: 0.22, 0.14, 0.11, and 0.43. Since the two classes of galaxies have a comparable distribution of apparent magnitudes, the S/Ns of the imaging used for the two subsamples is also comparable.

Finally, Figure 10 compares our SDSS parameters to those of Kormendy et al. (2009), who re-analyzed a subset of the ACSVCS galaxies, after discarding  $\sim 60$  of the 100 galaxies on the basis of visual morphological classification. Once again, the thin solid line in each panel shows the one-to-one relation while the dashed lines show least-squares fits:

$$\begin{aligned} V_{\text{K09}} &= (1.053 \pm 0.008)g \\ &\quad - (1.06 \pm 0.10) \quad \sigma = 0.14 \end{aligned}$$

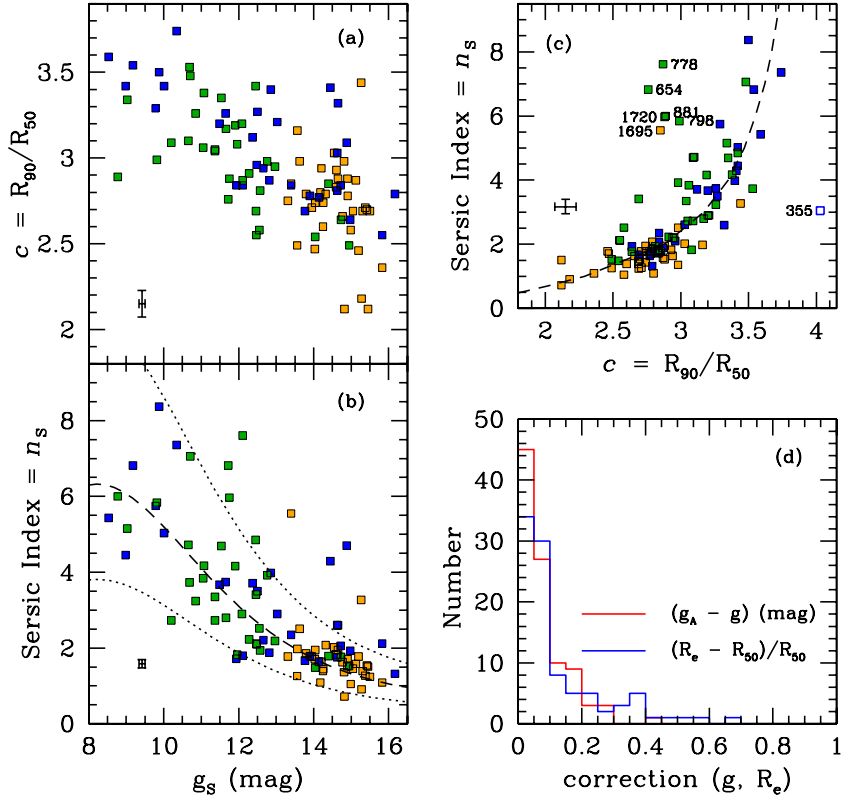


**Figure 7.** (a) Curve-of-growth concentration index,  $c$ , plotted as a function of total Sérsic magnitude,  $g_s$ . (b) Sérsic index,  $n_s$ , measured from the SDSS images plotted as a function of total magnitude; the dashed and dotted curves show the polynomial relations of P. Côté et al. (2010, in preparation). (c) Relationship between curve-of-growth concentration and Sérsic index. Several outlying galaxies are labeled, all of which either show multiple components (e.g., outer rings, bars, prominent large-scale disks, etc.) or have close companions that complicate the analysis. The dashed curve shows the expected relationship from Graham et al. (2005). (d) Histogram of the corrections applied to the curve-of-growth magnitudes and radii for the sample galaxies (see Section 3.1 for details).

(A color version of this figure is available in the online journal.)

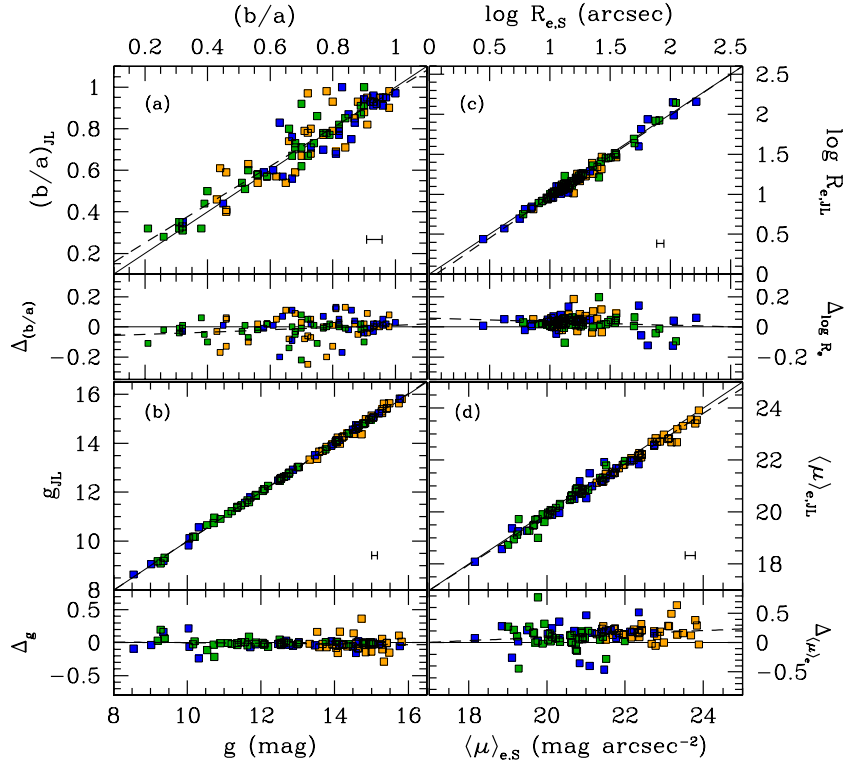


**Figure 8.** Comparison of our final curve-of-growth parameters to those of Janz & Lisker (2008). The thin solid line in each panel is the one-to-one relation, while the dashed line gives the line of best fit. The agreement between the two sets of measurements is excellent.

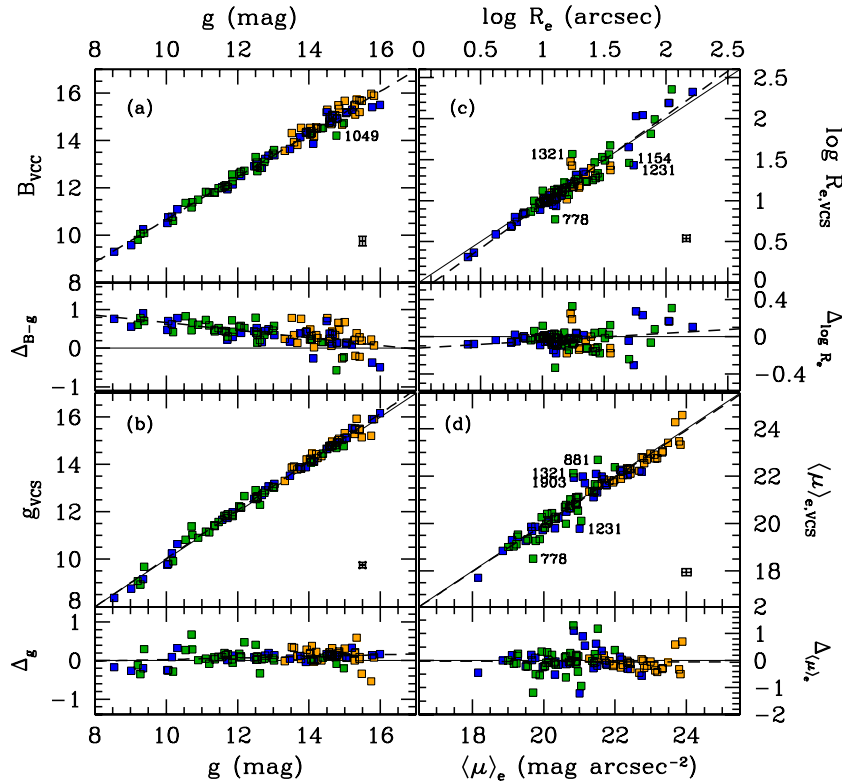


**Figure 9.** Comparison of our final curve-of-growth parameters to those from the VCC and ACSVCS. (a) Corrected curve-of-growth  $g$ -band magnitudes from SDSS plotted against  $B$ -band magnitude from Binggeli et al. (1985). The line shows a least-squares fit to the two data sets. (b–d) Comparison of total  $g$ -band magnitude, effective radius, and mean effective  $g$ -band surface brightness from our curve-of-growth analysis to those from the ACSVCS. The thin solid line in each panel shows the one-to-one relation, while the dashed line shows the best-fit linear relation. Overall, the SDSS curve-of-growth and  $HST$  Sérsic measurements show very good agreement for all three morphological groups.

$$\begin{aligned} \log n_{K09} &= (1.023 \pm 0.071) \log n_s \\ &\quad - (0.01 \pm 0.04) \quad \sigma = 0.12 \\ \log R_{e,K09} &= (1.124 \pm 0.031) \log R_e \\ &\quad - (0.11 \pm 0.04) \quad \sigma = 0.10 \\ \langle \mu \rangle_{e,K09} &= (1.022 \pm 0.058) \langle \mu \rangle_e \\ &\quad - (0.62 \pm 1.21) \quad \sigma = 0.43. \end{aligned} \quad (7)$$

The agreement is excellent, which is to be expected given that the Kormendy et al. (2009) sample was selected primarily to isolate “pure Es”: i.e., galaxies that, by definition, have the smoothest and most regular surface brightness profiles (this led to further rejection of four galaxies classified as S0s by Kormendy et al. 2009). Note, however, that 12 of the 25 (48%) galaxies reported as Es by Kormendy et al. (2009) are actually classified as either S0s or dwarfs by at least one of the classifiers used to compile the “consensus morphologies” reported in Table 1 and described in Section 3.2. Similarly, a small number (10) of dwarf galaxies (termed “spheroidals” in Kormendy et al. 2009) were also included in their sample, although there seems to be no clear criteria for discarding the remaining 25 “dwarf” galaxies in Table 1.

Issues of the subjectiveness of sample selection from morphology aside, the comparisons shown in Figures 6–10 demonstrate that it is possible to measure the basic parameters that describe the global structure of nearby early-type galaxies with quite reasonable accuracy, using different observational materials (ground-based versus  $HST$ ) with a dramatically different resolution (a factor of  $\sim 15 \times$  difference between ACS and SDSS), and using different techniques: non-parametric versus

simple three-parameter models that reproduce the gross profile shape through a scale normalization ( $R_e$ ), luminosity normalization ( $I_e$ ), and a global curvature index ( $n_s$ ). Nevertheless, some caution is probably advisable, as individual galaxies can present special challenges, particularly the largest and brightest objects.

To illustrate this point, Figure 11 shows our corrected, COG effective radii plotted against a variety of  $R_e$  measurements taken from the literature (as indicated by the legend in the upper left corner). The dashed line shows the one-to-one relation. Given that the literature measurements are rather heterogeneous in nature (e.g., measurements being made in a variety of bandpasses, spanning a wide range in angular resolution and spatial extent, and using both parametric and non-parametric approaches), it is perhaps not surprising that the comparison shows some scatter. However, as shown in the lower panel of this figure, the agreement is often best for the faintest and smallest galaxies; indeed, for  $R_e < 45''$ , the measurements are generally in good agreement aside from a handful of outlying measurements. For the dozen or so galaxies with  $R_e > 45''$ , the mean deviation  $\langle |R_{e,\text{lit}} - R_e| / R_e \rangle$  is  $0.37 \pm 0.12$ , or roughly 2.5 times that found for the smaller galaxies ( $0.15 \pm 0.08$ ).

As a rule, the greater the radial extent of the data used in the analysis, the larger the  $R_e$  measurements tend to be (e.g., Caon et al. 1990, 1994; Ferrarese et al. 2006a; L. Ferrarese et al. 2010, in preparation; Kormendy et al. 2009). For instance, the measurements of Alonso et al. (2003) are systematically smaller than most other measurements, being based on the total magnitude within  $R_{\max}$ , a radius corresponding to the  $1\sigma$  fluctuations in the sky brightness. For the  $\sim 10$  brightest galaxies, the COG measurements from our study and that of Burstein

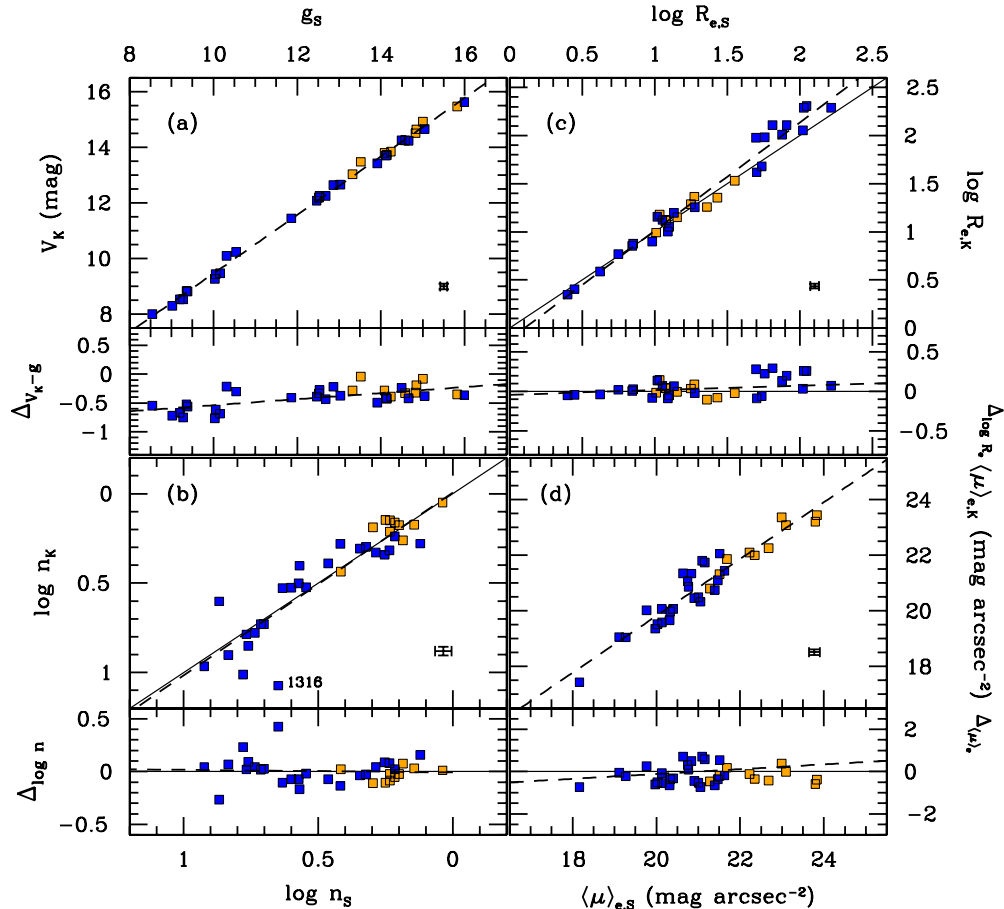


**Figure 10.** Comparison of the photometric and structural parameters derived from SDSS to those of Kormendy et al. (2009), who analyzed a subset of the 100 ACSVCS galaxies after excluding 60 galaxies on the basis of visual morphology. The thin solid lines in panels (b) and (c) show the one-to-one relations, while the dashed lines in all four panels show the best-fit linear relations. The galaxy with  $n = 11.84$  according to Kormendy et al. (2009) is VCC1316 (=M87). Note that the magnitudes in panel (a) and the surface brightness measurements in panel (d) refer to  $g$ -band measurements for the SDSS, and  $V$ -band values for Kormendy et al. (2009).

et al. (1987) are, on average,  $\sim 25\%$  smaller than the Caon et al. (1990, 1994), Ferrarese et al. (2006a), L. Ferrarese et al. (2010, in preparation), and Kormendy et al. (2009) values who fitted  $R^{1/4}$ -laws or Sérsic models to the one-dimensional surface brightness profiles. Although we have taken care to estimate the “background” surface brightness for these large galaxies by using wide-field ( $1^\circ \times 1^\circ$ ) mosaics, we cannot rule out the possibility that the sky values have been slightly overestimated for these highly extended galaxies. In any event, we conclude that the measurement of accurate sizes for the brightest galaxies remains a challenge, with published results being dependent on the technique and/or parameterization used in the analysis.

### 3.2. Photometric and Structural Scaling Relations

The intrinsic properties of early-type bright and faint galaxies—and the relationship between these apparently distinct classes—has been a subject of debate for several decades. From analysis of the magnitude–size and magnitude–surface brightness relations for galaxies in the Virgo Cluster, Sandage & Binggeli (1984) and Binggeli et al. (1984) noted an inflection between the E and dE sequences at  $B_T \sim 13$ , although they argued that the dwarfs defined the low-luminosity extension of the giant elliptical sequence. Shortly afterward, Kormendy (1985) reported the discovery of two diverging, and nearly orthogonal, sequences at  $M_B \sim -17$  ( $B \sim 14$  in Virgo) mag in the scaling relations between central surface brightness, core radius,

and total luminosity (see his Figure 3). The sense of this apparent “dichotomy” is such that the central surface brightness of dwarf ellipticals *increases* with increasing galaxy luminosity, whereas these parameters appear anti-correlated in the giants, leading Kormendy (1985, p. 77) to conclude that “dwarf spheroidals and ellipticals formed in very different ways.” However, a number of researchers have since suggested that the apparently strong discontinuity in the sample analyzed by Kormendy (1985) may have been due to the modest sample size ( $\approx 30$  galaxies in total) and the paucity of galaxies at the absolute magnitude of the claimed dichotomy (see, e.g., Binggeli & Cameron 1993; Jerjen & Binggeli 1997; Graham & Guzmán 2003).

These studies have generally argued for a smoother, nearly continuous transition between giant and dwarf galaxies. Graham et al. (2003), using surface brightness data for a larger sample of galaxies, many of which were observed with high angular resolution with *HST*, found no evidence for a dichotomy in the  $M_B - \mu_0$  relation, but rather, a systematic and nearly linear increase in central surface brightness with magnitude (aside from the highest luminosity galaxies, whose central surface brightness is thought to have been reduced as a result of binary black hole interactions; Ebisuzaki et al. 1991; Faber et al. 1997; Milosavljević & Merritt 2001). A similar conclusion has been reached by Misgeld et al. (2008, 2009) for early-type galaxies in the Hydra I and Centaurus Clusters. In a study of galaxies in the Perseus Cluster and other environments, de

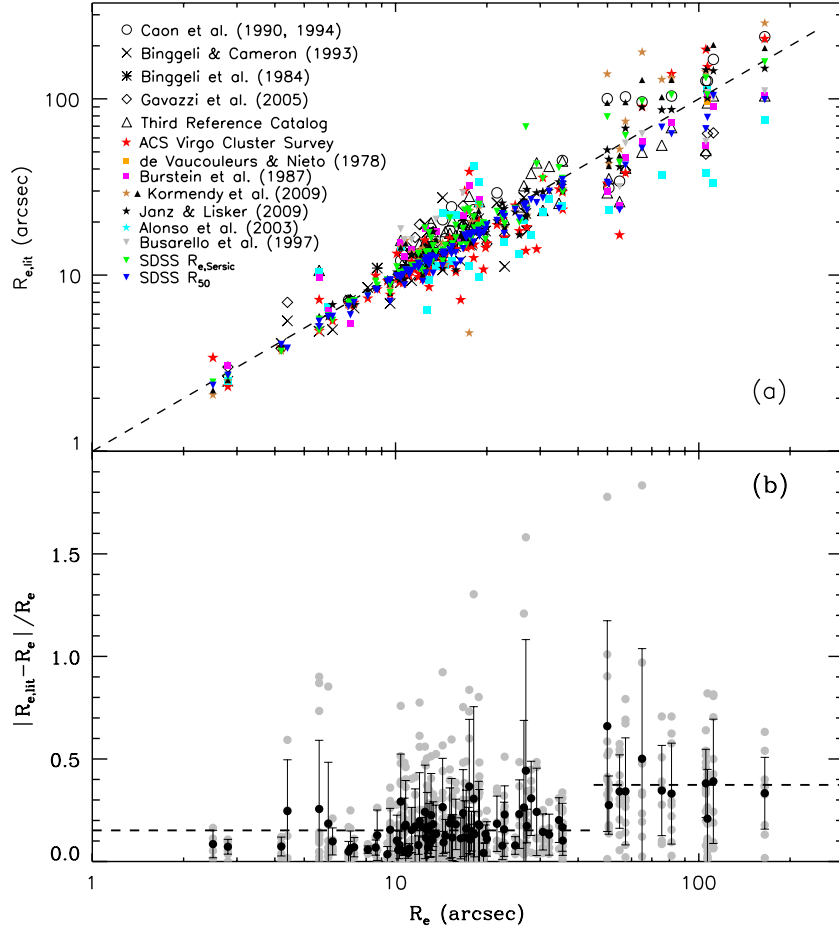


**Figure 11.** (a) Effective radius measurements from the SDSS curve-of-growth analysis ( $R_e$ ) compared to other determinations in the literature ( $R_{e,\text{lit}}$ ; Caon et al. 1990, 1994; Binggeli & Cameron 1993; Binggeli et al. 1984; Gavazzi et al. 2005; Third Reference Catalog; ACS Virgo Cluster Survey; de Vaucouleurs & Nieto 1978; Burstein et al. 1987; Kormendy et al. 2009; Janz & Lisker 2009; Busarello et al. 1997). The dashed line shows one-to-one relation. For galaxies with  $R_e \lesssim 45''$ , the different measurements are generally in agreement. However, for the brightest and most extended galaxies, there can be large discrepancies. (b) Gray dots show the fractional error in the effective radius measurements,  $|R_{e,\text{lit}} - R_e| / R_e$ , plotted as a function of the SDSS effective radii; the mean and standard deviation for individual galaxies are plotted as the black dots with error bars. The dashed lines show the mean values for the galaxies divided at  $R_e = 45''$  ( $0.15 \pm 0.08$  vs.  $0.37 \pm 0.12$ ). This comparison demonstrates that the measured sizes of the brightest galaxies are often both uncertain and model dependent.

(A color version of this figure is available in the online journal.)

Rijcke et al. (2009) used *HST* data to measure half-light radii, central surface brightness, and Sérsic indices for a sample of early-type systems, concluding that “all these parameters vary in a continuous fashion with galaxy luminosity over a range of more than six orders of magnitude in luminosity.” In the specific case of the Virgo Cluster, several studies have also found smooth, nearly continuous relation in structural parameters (e.g., Jerjen & Binggeli 1997; Barazza et al. 2003; Gavazzi et al. 2005; Ferrarese et al. 2006a). Moreover, Zaritsky et al. (2006a, 2006b, 2008), Wolf et al. (2010), and Tollerud et al. (2010) have recently shown that the mass-based scaling relations of (mostly early-type) galaxies appear to extend continuously across the mass scale marking the apparent dichotomy of Kormendy (1985). On the other hand, a recent analysis of the size–magnitude radius relation for Virgo early-type galaxies (Janz & Lisker 2008) did indeed describe the size–magnitude relations in terms of a dichotomy (contrary to findings from an analysis of the CMR; Janz & Lisker 2009, see also Section 3.4). However, the nature of the distinction of the giants and dwarfs in the size–magnitude plane noted by Janz & Lisker (2008)—i.e., systematic residuals in effective radius in the range  $-20 \lesssim M_r \lesssim -17$  that depart from the mean relation by a factor of about 1.5 in opposite senses—is a far more subtle difference than the  $\sim 10^4$

discrepancy in central surface brightness that originally led to the notion of a “dichotomy” between E and dwarf galaxies (see the upper right panel of Figure 3 from Kormendy 1985).

We revisit this issue of a structural dichotomy between “giant” and “dwarf” galaxies using the non-parametric photometric and structural parameters derived above. Panels (a) and (b) of Figure 12 show the  $R_e - M_g$  and  $\langle \mu \rangle_e - M_g$  scaling relations of our program galaxies where absolute magnitudes,  $M_g$ , were derived using the recalibrated surface brightness fluctuations (SBF) distances from Blakeslee et al. (2009), with the mean Virgo Cluster distance of 16.5 Mpc (Mei et al. 2007) adopted for galaxies without a direct SBF measurement. To better explore the trends with galaxy luminosity, we include in Figure 12 all galaxies<sup>11</sup> from the INT study of Gavazzi et al. (2005), shown as brown symbols, that do not appear in our sample: i.e., 204 galaxies, bringing the total number of galaxies in Figure 12 to 302 (i.e., excluding VCC355 and VCC1327 from the SDSS sample; see Section 3.1). Since Gavazzi et al. (2005) tabulate

<sup>11</sup> Gavazzi et al. (2005) restrict their analysis to morphological types E and dE, meaning that S0 galaxies will be somewhat underrepresented in the combined sample. As we show below, the S0 galaxies have global structural parameters that are intermediate to those of the Es and dEs; see also Janz & Lisker (2008).

effective major-axis radii, we have transformed their values into geometric mean effective radii by using the mean axial ratios from the VCC. We adopt a Virgo distance of 16.5 Mpc and convert the Gavazzi et al. (2005)  $B$ -band magnitudes into the  $g$  band assuming  $(B - g) = 0.42$  mag which should be appropriate for these old, low-mass systems (e.g., P. Côté et al. 2010, in preparation). The dashed curve in panel (c) shows the completeness fraction,  $f_c$ , of our final sample of Virgo early-type galaxies, derived from the catalog of Binggeli et al. (1985) by adopting a distance of 16.5 Mpc for all certain or probable Virgo members without an SBF distance. As mentioned in Section 1, the ACSVCS sample itself is fully complete for early-type galaxies brighter than  $M_g \approx -19.8$  and about 60% complete  $M_g \lesssim -15.8$ . In total, the sample of 302 early-type galaxies shown in Figure 12 constitutes  $\approx 43\%$  of the early-type galaxy population in the catalog of Binggeli et al. (1985) down to  $B_{\text{VCC}} \approx 19$ . Generally speaking, our early-type completeness fraction decreases steadily with magnitude, with localized dips at  $M_g \approx -19, -17.7$  and  $-15.4$ .

As before, the SDSS program galaxies in Figure 12 have been divided according to the “consensus morphologies” in Table 1.<sup>12</sup> All but two of the Gavazzi et al. (2005) galaxies shown in Figure 12 are classified in Binggeli et al. (1985) as dE galaxies (brown circles); the two galaxies classified as Es (VCC1148 and VCC1521) are shown as brown squares. Recall from Section 3 that the SDSS galaxies with uncertain morphological types, or having primary classifications (i.e., E versus S0, E or S0 versus dwarf, etc.) that differ significantly amongst the classifiers, are indicated by a colon (:). A total of 50 of the 100 galaxies fall into this category—a clear reflection of the subjective nature of the classification process—so caution is advisable when interpreting these classifications for individual galaxies. Nevertheless, by grouping the galaxies into three broad bins, we can hope to highlight the basic trends with morphology, should any such trends exist. One point, however, is immediately clear: given the uncertainty in the morphological classifications, it is obviously advisable to first characterize the scaling relations with samples that have the highest possible levels of completeness, and *then* consider how—or if—culling by morphology alters the observed relations.

The smooth curves in panels (a) and (b) show the expected trends for galaxies with Sérsic-like profiles, as given in Côté et al. (2010). Note that these are based on the  $\mu_0$ - and  $n$ -magnitude relations derived from Sérsic model fits to the azimuthally averaged brightness profiles for  $\sim 400$  galaxies in Virgo, Fornax, and the Local Group. As pointed out in Côté et al. (2010), the global relations are expected to vary smoothly over the magnitude range shown here, including the characteristic “bend” near  $M_g \sim -18$ . The inflection at this magnitude is a consequence of the non-homologous structure of the galaxies—a point first noted in Section 4 of Graham & Guzmán (2003)—which show a gradual but unmistakable change in their internal structure with luminosity: i.e., from  $n_S \gtrsim 4$  at the high-luminosity end of the early-type luminosity function, to  $n_S \sim 1$  for the low-luminosity (“dwarf”) galaxies. This variation, which was noted in Section 5.3 of Ferrarese et al. (2006a) and in a number of earlier studies (e.g., Jerjen & Binggeli 1997; Binggeli & Jerjen 1998; Barazza et al. 2003; Gavazzi et al. 2005), is confirmed here using the SDSS-based parameters (see again Figure 7(b)).

<sup>12</sup> These classifications are taken from the following sources: Reaves (1983), Binggeli et al. (1985), RC3 (de Vaucouleurs et al. 1991), and van den Bergh (P. Côté et al. 2010, in preparation).

The behavior of the scaling relations below this inflection point—where those galaxies classified as dwarfs dominate the overall early-type population (e.g., Sandage et al. 1985; Binggeli et al. 1988)—is worth examining more closely. In the lower panels of Figure 12, we show histograms of the residuals, with respect to the smooth curves in panels (a) and (b), in  $\log R_e$  and  $\langle \mu \rangle_e$  for all galaxies with  $M_g \gtrsim -18.5$ . Galaxies are again divided on the basis of morphology, with Es, S0s, and dwarfs shown in blue, green, and orange, respectively; residuals for the sample of faint dwarfs from Gavazzi et al. (2005) are shown in brown. It is worth recalling that the classifications are in many cases ambiguous, with considerable disagreement over the exact morphological typing from visual inspection alone (see above). If we nevertheless take the morphological classifications at face value, we find a tendency for the faint galaxies classified as Es to have smaller sizes and higher surface brightnesses than the faint S0s, which are in turn smaller and of higher surface brightness than the dwarfs (see also Figures 1 and 2 of Janz & Lisker 2008). This tendency can be understood as a consequence of morphological classification schemes—including that of the VCC (Sandage & Binggeli 1984; Binggeli et al. 1985)—in which galaxies with low surface brightness are classified as dwarfs while E galaxies are identified as those objects with relatively high surface brightness; S0/dS0 galaxies generally have intermediate properties. To illustrate this point, we show how lines of constant  $\langle \mu \rangle_e$  (the vertical gray lines drawn at 20.5, 21.5, and 22.5 mag arcsec $^{-2}$  in panel b) and their equivalents in  $\log R_e$  appear in the range  $-18.5 \lesssim M_g \lesssim -14.5$ , where the ambiguity between “giants” and “dwarfs” is most problematic.

What seems clear from Figure 12 is that the galaxies fainter than  $M_g \sim -18.5$  (corresponding to a stellar mass of roughly  $\sim 10^{10} M_\odot$  for a Chabrier initial mass function (IMF); e.g., Peng et al. 2008) show broad distributions in their global parameters rather than neatly dividing into two distinct populations. For instance, if we divide the SDSS sample at  $M_g \sim -18.5$ , the rms scatter about the fitted relations in both panels of Figure 12 is  $2.1 \times$  larger at the low-mass end. Much of this increased scatter is due to a few extreme examples of the E and, to a lesser extent, dwarf classes. If, for the time being, we restrict ourselves to the 58 galaxies fainter than  $M_g \sim -18.5$ , then three interesting points are worth making. First, as summarized in Table 4 (which gives the mean and standard deviation of  $R_e$  and  $\langle \mu \rangle_e$  for each of the three subsamples of SDSS galaxies studied here), the distributions of effective radius and effective surface brightness are clearly overlapping between the E, S0, and dwarf samples (as noted in the above paragraph; see also Figure 1 of Janz & Lisker 2008), with clear differences in the mean, but no evidence for a dichotomy. Second, galaxies that are less centrally concentrated and have lower surface brightness are generally thought of as dwarfs, while galaxies that are more highly concentrated and have higher surface brightness are generally classified as giants (Es or S0s).<sup>13</sup> However, such a posteriori classifications are *by design*, and, when the population of low-luminosity galaxies as a whole is considered, there is no indication of two distinct and

<sup>13</sup> The approximate dividing points are  $R_e \sim 800$  pc and  $\langle \mu \rangle_e \sim 21.5$  mag arcsec $^{-2}$ . For example, if we consider the 55 galaxies in the range  $-18 \leq M_g \leq 16$ , the distribution of morphological types in the  $\log R_e$ – $M_g$  plane with respect to an effective surface brightness of  $\langle \mu \rangle_e(\text{trans}) = 21.5$  mag arcsec $^{-2}$  is a surprisingly accurate reflection of their morphological classifications: e.g.,  $(35/39) = 90\%$  of dwarfs have  $\langle \mu \rangle_e > \langle \mu \rangle_e(\text{trans})$ , while  $(9/12) = 75\%$  of Es have  $\langle \mu \rangle_e < \langle \mu \rangle_e(\text{trans})$ , as do  $(3/4) = 75\%$  of S0s.

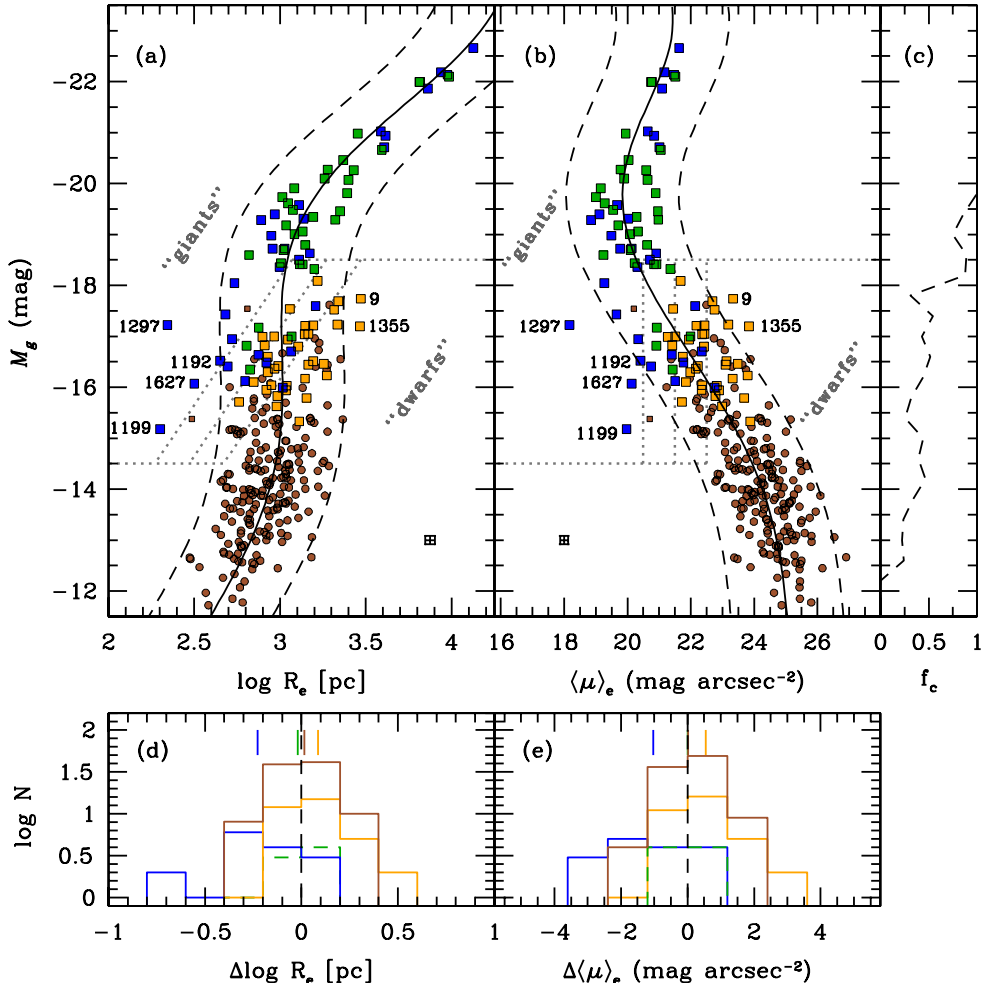


**Figure 12.** Relationship between absolute  $g$ -band magnitude and effective radius,  $R_e$ , and mean  $g$ -band effective surface brightness,  $\langle \mu \rangle_e$  (panels (a) and (b), respectively) for ACSVCS galaxies (squares). The brown circles and squares show the 204 galaxies (dEs and Es, respectively) from the survey of Gavazzi et al. (2005) that do not appear in our sample. The smooth curves in the two panels show the polynomial relations and  $\pm 2\sigma$  limits from P. Côté et al. (2010, in preparation). A number of outlying ACSVCS galaxies have been labeled. The dashed lines drawn between  $M_g = -18.5$  and  $-14.5$  in panels (a) and (b) show lines of constant effective surface brightness,  $\langle \mu \rangle_e = 20.5, 21.5$ , and  $22.5$  mag arcsec $^{-2}$ . The approximate completeness fraction,  $f_c$ , of our sample of Virgo early-type galaxies (from Binggeli et al. 1985) is shown as the dashed curve in panel (c), where a mean distance of 16.5 Mpc has been adopted for galaxies without direct distance measurements in Blakeslee et al. (2009). (d) Residuals of effective radii around the smooth curve in panel (a) for galaxies fainter than  $M_g = -18.5$ . The vertical lines show the mean residuals for the different morphological types, as well as for the Gavazzi et al. (2005) sample, which is comprised overwhelmingly of dwarf galaxies. (e) The same as panel (d), except showing the residuals in effective surface brightness.

(A color version of this figure is available in the online journal.)

non-overlapping populations.<sup>14</sup> Finally, there are  $\approx$ four galaxies with very small  $R_e$  and high  $\langle \mu \rangle_e$  that define an extended tail to the galaxy distribution; given their rather extreme properties, these systems have in the past invariably been classified as Es or compact ellipticals (cEs). While these galaxies—VCC1297, VCC1192, VCC1627, and VCC1199—seem to fall roughly along a linear extrapolation of the sequence defined by the most massive E/S0s (see, e.g., Figure 2 of Dabringhausen et al. 2008), there are reasons to believe that these rare objects are offset from the smooth curves defined by the great majority of early-type galaxies because of environmental effects, as we now discuss.

Figure 13 explores how the residuals from the smooth curves in Figure 12 vary with position in the Virgo Cluster.

<sup>14</sup> Some recent studies have noted the fact that ultra-compact dwarf galaxies and compact ellipticals appear to fall along the extrapolation of the E sequence (e.g., Haşegan et al. 2005; Dabringhausen et al. 2008; Chilingarian et al. 2009; Price et al. 2009; Côté et al. 2010), although in no case are these results described as a dichotomy. Rather, the most common interpretation is that these compact, low-mass systems may be the end products of “galaxy threshing” or tidal stripping (e.g., Faber 1973a; Bekki et al. 2001a, 2001b).

**Table 4**  
Global Structural Parameters for Low-luminosity Galaxies

Parameter	E	S0	Dwarf
$N$	15	8	35
$\log R_e$ (pc)	$2.77 \pm 0.26$	$3.00 \pm 0.15$	$3.10 \pm 0.17$
$\langle \mu \rangle_e$ (mag arcsec $^{-2}$ )	$20.73 \pm 1.25$	$21.07 \pm 0.52$	$22.55 \pm 0.75$

Residuals are plotted against projected distance from M87 or M49—whichever is smaller—as these two E galaxies mark the respective centers of the Virgo A and B subclusters (see Binggeli et al. 1987; Binggeli & Popescu 1995; Schindler et al. 1999; Mei et al. 2007). The symbols are the same as in the previous figure, with the exception of the bright galaxies ( $M_g \lesssim -18.5$ ) which are now plotted as open squares. Among the faint sample, there is a trend in both the  $R_e$ – $M_g$  and  $\langle \mu \rangle_e$ – $M_g$  relations for the most extreme E-type (=cE) galaxies to lie close to the centers of the A or B subclusters: i.e., in close proximity to either M87 or M49 (or, in the case of VCC1627, M89).

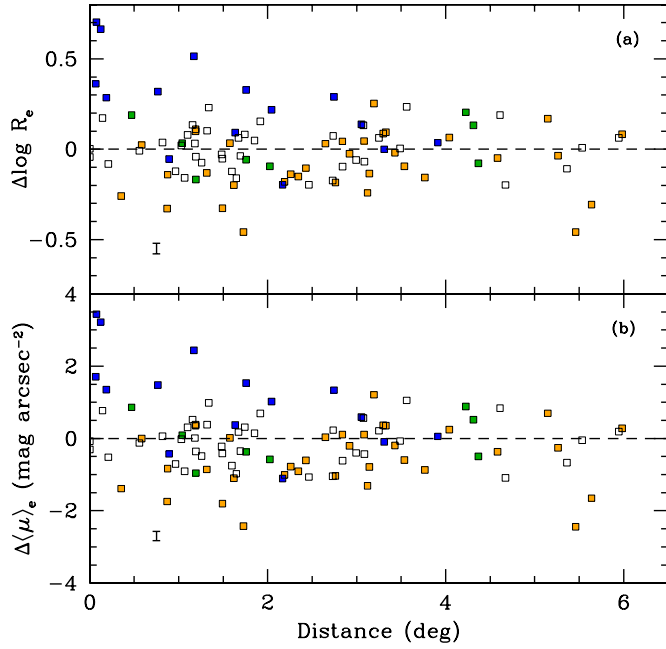


**Figure 13.** (a) Offset from the  $\log(R_e)$ – $M_g$  relation in Figure 12 plotted against the distance from M87 or M49—whichever is smaller. These luminous galaxies mark the centers of the Virgo A and B subclusters (Binggeli et al. 1987). Open symbols show galaxies brighter than  $M_g = -18.5$ ; fainter galaxies are divided into three morphological bins as explained in Section 3. (b) Same as above, except using the  $\langle\mu\rangle_e$ – $M_g$  relation in Figure 12. Note the tendency for compact, high-surface brightness galaxies (classified as Es or cEs) to be found in the cores of the A and B subclusters.

It has been argued on theoretical grounds many times in the past that cEs are created by tidal stripping of intermediate-mass progenitors (e.g., King 1962; Faber 1973a; Keenan & Innanen 1975; Bekki et al. 2001b). Our observations are in support of this picture. Meanwhile, as Figure 13 also shows, the most diffuse dwarf galaxies also tend to be found in the low-density outskirts of the cluster and are thus candidates for infalling galaxies whose internal structures have yet to be modified by galaxy–galaxy encounters (Moore et al. 1996). This is consistent with the findings of Lisker et al. (2007) who found a wide variety of dwarf galaxy shapes, with an apparent morphology–density relation within the cluster.

In summary, the evidence at hand does not favor a structural dichotomy of the sort proposed by Kormendy (1985), but rather, a gradual variation in the structural properties of early-type galaxies along the luminosity function, including an “inflection” at  $M_g \sim -18$  that arises from structural non-homology. Below this bend, galaxies follow the general trends expected for the measured variation in the Sérsic index with magnitude, although there is a clear scatter about the relation that is probably a reflection of the different physical processes that have been most important in shaping the structure of individual galaxies (i.e., dissipation, harassment, tidal stripping, etc.). For obvious reasons, progress toward elucidating these mechanisms and assessing their relative importance will require detailed observations of individual galaxies, but we emphasize that it is important to select such galaxies in a quantitative fashion using carefully selected and unbiased samples. We suggest that location in the cluster color–magnitude diagram (see Section 3.4), rather than visual morphology, may offer an attractive route forward as it is possible to select, with little or no ambiguity amongst researchers, objects belonging to the red-sequence or blue cloud populations that correspond roughly to the early-

/late-type classifications that have been historically used in the study of nearby galaxies.

### 3.3. Axial Ratios, Ellipticities, and Intrinsic Shapes

Another observable that may offer a clue into the possibility of distinct populations within the sample of early-type galaxies studied here is the distribution of axial ratios. The intrinsic shapes of giant early-type galaxies (i.e., Es and S0s) has a long history, being the focus of many previous works (e.g., Sandage et al. 1970; Rix & White 1990, 1992; Lambas et al. 1992; Jørgensen & Franx 1994; Michard 1994; van den Bergh 1994). Less attention has been devoted to early-type dwarfs as a class, although a few investigators have addressed this problem, including, in a few instances, the specific case of dwarfs in the Virgo Cluster (e.g., Binggeli & Cameron 1991, 1993; Binggeli & Popescu 1995; Ryden et al. 1999), or in Fornax (Ferguson & Sandage 1989). Very recently, SDSS imaging has been used to study the intrinsic shapes for a large sample of early-type dwarfs selected from the VCC (e.g., Lisker et al. 2007, Lisker et al. 2009; see also Janz & Lisker 2008). The brief analysis that follows is complementary to those studies, but is based on fewer galaxies (100 in total, compared to  $\approx 450$  dwarfs examined in Lisker et al. 2007, Lisker et al. 2009) so we refer the reader to those comprehensive studies for more details.

We begin by showing in Figure 14 the relationship between ellipticity measured from the SDSS imaging,  $\epsilon = 1 - (b/a)$ , absolute magnitude,  $M_g$ ,  $(u-z)$  color (Section 3.4), and position within the cluster. Panel (a) shows the familiar result (e.g., van der Wel et al. 2009) that the brightest galaxies (which are primarily, but not exclusively, classified as Es) have generally low ellipticities (mean  $= 0.18 \pm 0.08$ ). Fainter than  $M_g \sim -21$ , many galaxies of comparably low ellipticities may be found in the cluster, although the distribution in this regime extends to significantly higher values—up to  $\sim 0.8$  in a few cases. At progressively fainter magnitudes, these extremely elongated systems evidently disappear. We note that the most flattened systems (i.e.,  $\epsilon \geq 0.5$ ) include galaxies of all morphological types, not just S0 galaxies. The gray circles with error bars in panel (a) show the mean and standard deviations as a function of galaxy magnitude, illustrating these general trends (Table 5).

Panel (b) of Figure 14 shows the ellipticity–color relation for the sample galaxies. As was the case with Figure 13, galaxies brighter than  $M_g = -18.5$  are plotted here using open squares. For these giant galaxies, there is little or no correlation between  $(u-z)$  color and mean ellipticity, a consequence of the fact that these systems lie on the upper part of the red sequence where galaxies have nearly constant color:  $\langle(u-z)\rangle = 3.16 \pm 0.15$  (see Section 3.4). For fainter galaxies, however, there is a significant correlation between color and ellipticity, with  $(u-z) = (2.71 \pm 0.08) - (0.54 \pm 0.23)\epsilon$  for just the dwarfs (blue dot-dashed line), and  $(u-z) = (2.81 \pm 0.07) - (0.65 \pm 0.21)\epsilon$  if no selection on morphological type is imposed (red long-dashed line). Thus, for galaxies in the luminosity regime that is typically identified with dwarf galaxies, there is a clear trend in the sense that the most flattened systems tend to have bluer colors. This would be consistent once again with expectations from theory that, as low-mass galaxies with disk-like structures fall into the cluster and undergo repeated high-speed encounters with the other galaxies—and respond to tidal effects from massive galaxies and the cluster itself—they are depleted of their large-scale reservoir of gas and transformed into passively evolving, spheroidal systems (e.g., Gunn & Gott 1972; Larson et al. 1980; Moore et al. 1996). In panel (c), we show the dependence of

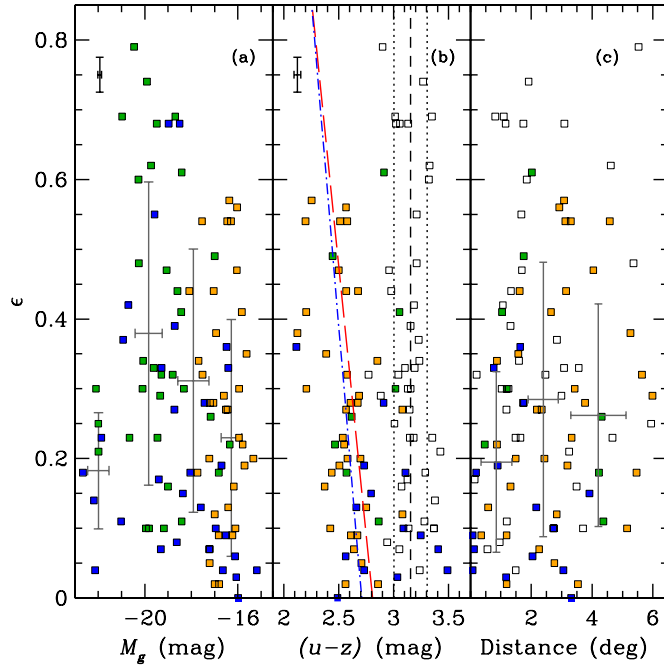


**Figure 14.** (a) Relationship between measured ellipticity,  $\epsilon = 1 - (b/a)$ , and absolute  $g$ -band magnitude. The gray error bars show the mean trends as a function of galaxy magnitude. Galaxies brighter than  $M_g \sim -21$  have rather low ellipticities,  $(\epsilon) \approx 0.18 \pm 0.08$ . Fainter galaxies have a wider range in ellipticity with an average value that decreases slowly with decreasing galaxy luminosity, irrespective of morphological type. (b) Relationship between ellipticity and  $(u-z)$  color. In this panel, galaxies brighter than  $M_g = -18.5$  are shown by open symbols. The dashed and dotted lines show the roughly constant color and  $\pm 1\sigma$  confidence limits for these high- and intermediate-luminosity galaxies. Fainter galaxies show a trend in the sense that more flattened galaxies have bluer colors; the blue, dot-dashed line shows the least-squares fit for just the dwarf galaxies, while the red, long-dashed line shows the best-fit relation for all galaxies with  $M_g \geq -18.5$ . (c) Ellipticity plotted as a function of distance from the centers of either the A or B subclusters, as in Figure 13. The gray error bars show the mean trends for galaxies with  $M_g \geq -18.5$ .

(A color version of this figure is available in the online journal.)

**Table 5**  
Ellipticities for Program Galaxies

$M_g$	$N$	$\langle \epsilon \rangle$ (mag)
$-22.00 \pm 0.46$	8	$0.18 \pm 0.08$
$-19.83 \pm 0.59$	25	$0.38 \pm 0.22$
$-17.92 \pm 0.67$	32	$0.31 \pm 0.19$
$-16.28 \pm 0.45$	35	$0.23 \pm 0.17$

ellipticity as a function of distance from the centers of either the A or B subclusters, as marked by M87 or M49. For the sample of faint galaxies ( $M_g \geq -18.5$ ), there is a subtle but real tendency for the most flattened galaxies to be found at large or intermediate distances, and to be absent in the subcluster cores. Conversely, the roundest low-mass galaxies are found exclusively in the inner regions of the subclusters, with no systems having  $\epsilon < 0.1$  found beyond  $\sim 4^\circ$  (1.15 Mpc).

In Figure 8(a), we compared our measurements of the axial ratios to those from Janz & Lisker (2008). While the excellent agreement found there is reassuring, it is perhaps not surprising given that both sets of measurements were performed on the same SDSS images. However, an important independent check on our measurements is available from the ACSVCS which has the advantage of much superior angular resolution, albeit with a reduced field of view. In Figure 15, we compare our

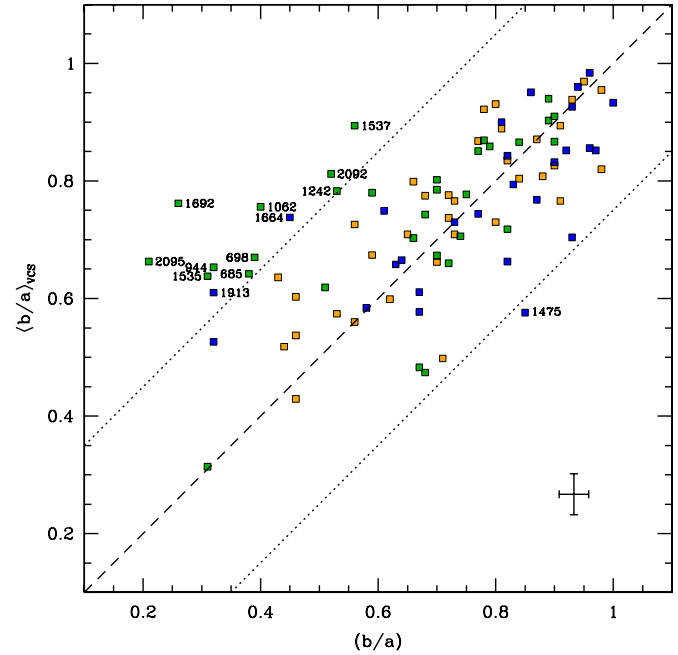


**Figure 15.** Comparison of axial ratios,  $(b/a)$ , measured from the SDSS to those from the ACSVCS. The dashed line shows the one-to-one relation with offsets of  $\pm 0.25$  indicated by the dotted lines. Galaxies whose measurements in the two data sets differ by more than this amount are labeled, most of which are intermediate-luminosity systems classified as S0s. Note that VCC1475, which is nominally classified as an E galaxy, shows an inner disk-like structure in the ACS imaging (see Figure 23 of Ferrarese et al. 2006a).

SDSS axial ratios to those from the ACSVCS (Ferrarese et al. 2006a; L. Ferrarese et al. 2010, in preparation). The dashed line shows the one-to-one relation, with offsets of  $\pm 0.25$  indicated by the dotted lines. For the most part, there is good agreement between the measurements, although there are some outliers. Most of these are classified as S0 galaxies and deviate in the same sense: i.e., the SDSS axial ratios are higher (by roughly a factor of  $\sim 2$ ) than those found using the ACS images. Recall, however, that the SDSS values are measured at the  $5\sigma$  isophote, while the ACSVCS values are mean values measured between  $1''$  and  $R_e$  (Ferrarese et al. 2006a). We have confirmed that the discrepancies for these galaxies are due to the different radial ranges used in the analysis, coupled with a radial variation in the ellipticity profile for these particular galaxies: i.e., if we remeasure, using the F475W images from the ACSVCS, the axial ratios of the outlying galaxies in Figure 15 at the radii corresponding to the  $5\sigma_{\text{sky}}$  isophotes determined from the SDSS images, we find the mean absolute deviation in the axial ratio measurements is found to be  $| (b/a)_{\text{SDSS}} - (b/a)_{\text{ACSVCS}} | = 0.10 \pm 0.12$ .

Finally, we present in Figure 16 the distribution of ellipticities for galaxies classified as Es, S0s, and dwarfs in panels (a) through (c), respectively. The solid and dashed histograms in each panel show the results obtained using the SDSS and ACSVCS measurements. Overall, the distributions look similar, although there is a tendency for the ACS distributions to show fewer highly elongated galaxies. These distributions can be compared to the distributions of E, S0, and spiral galaxies from the APM survey of Lambas et al. (1992), who noted that purely oblate or prolate populations cannot account for the observed E distribution, arguing instead for mild triaxiality in this population. Note that we have chosen to compare the dwarfs in panel (c) with the APM spirals since the nearly exponential

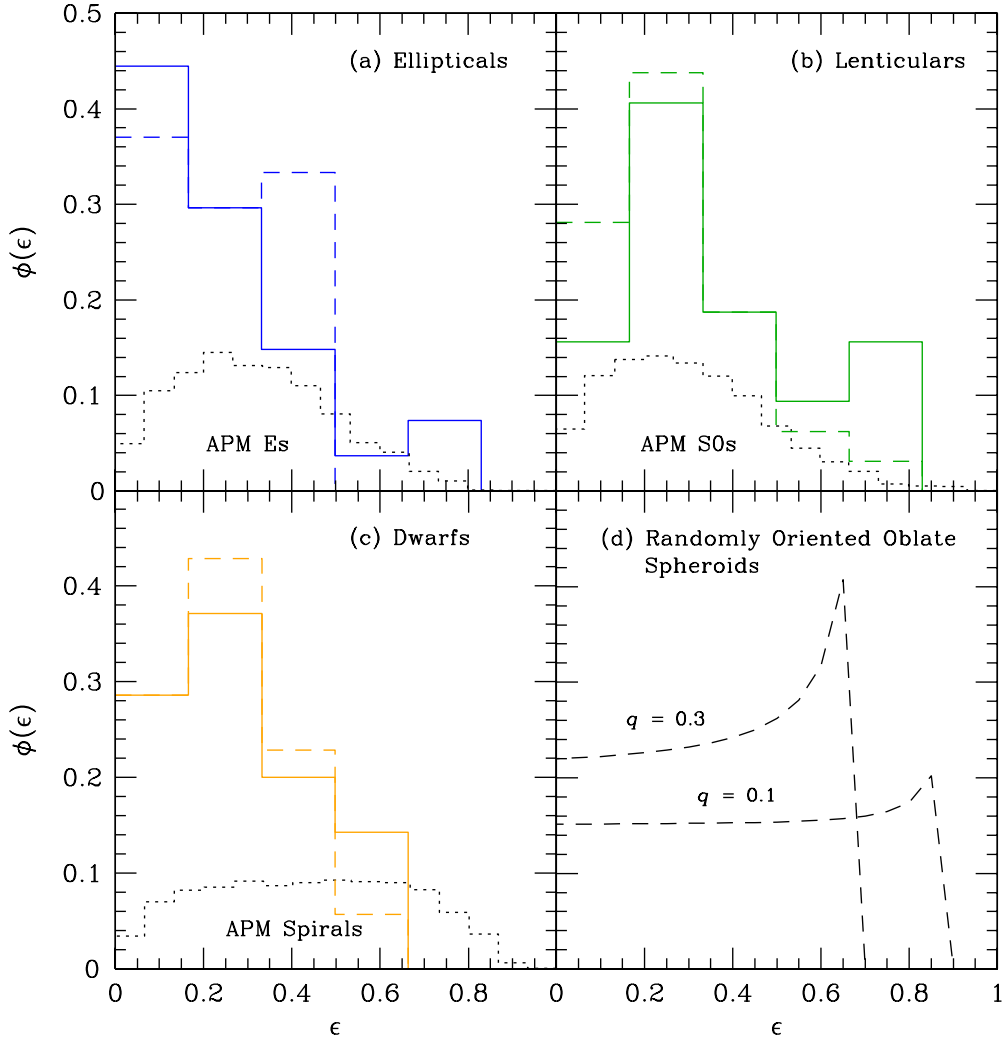


**Figure 16.** Distribution of ellipticities based on the SDSS imaging, divided according to the morphologies in Table 1. In each panel, the solid and dashed histograms show the results from the SDSS and ACSVCS analyses, respectively. The dotted black histograms in panels (a)–(c) show the distributions for Es, S0s, and spirals from the APM survey of Lambas et al. (1992). Panel (d) shows the distributions expected for randomly oriented oblate spheroids, with intrinsic axial ratio  $q \equiv b/a$ . Note the poor agreement with the dwarf galaxy distribution, demonstrating that the great majority of these low-mass systems are not thin disks.

(A color version of this figure is available in the online journal.)

surface brightness profiles of these galaxies (Figure 7; Ferrarese et al. 2006a) has been taken as suggestive of a connection to disks (Kormendy 1985). However, this comparison reveals a poor match of the dwarf distribution to that for the APM spiral galaxies, as it peaks at low ellipticity ( $\approx 0.25$ ) and contains no systems more flattened than  $\langle \epsilon \rangle \sim 0.65$ . This is true for both the *HST* or SDSS measurements. It may be that, as noted by Binney & de Vaucouleurs (1981), low-mass dwarfs are less flattened than expected because of more isotropic velocity distributions resulting from relatively large ratios of random to rotational kinetic energy.

The final panel of Figure 16 shows this result in a different way, comparing to the distribution expected for a population of oblate spheroids viewed at random inclination angles (Giovanelli et al. 1994):

$$\phi(\epsilon) = (1 - \epsilon)/\sqrt{[(1 - \epsilon)^2 - q^2](1 - q^2)}. \quad (8)$$

Here  $q \equiv b/a$  is the intrinsic axial ratio of the spheroid. We show in Figure 16 this distribution for two cases ( $q = 0.1$  and  $0.3$ ) to illustrate the behavior expected for highly flattened systems. As in panel (c), there is poor agreement with the

observed distributions for dwarf galaxies—further evidence that these low-mass systems, despite their having nearly exponential surface brightness profiles, are not bona fide disk galaxies, although a few prime candidates for such galaxies certainly exist, most notably VCC856 and VCC1695 which show weak, face-on spiral patterns; Jerjen et al. 2000; Ferrarese et al. 2006a; Lisker et al. 2006; Lisker & Fuchs 2009).<sup>15</sup> We note here that, of the 35 galaxies in Table 1 which are classified as dwarfs, only 6 are listed as possible dS0 systems in the VCC, with the remaining galaxies classified as dEs (either of the nucleated or

<sup>15</sup> VCC856 and VCC1695 are classified in Binggeli et al. (1985) as dE1, N, and dS0: galaxies, respectively. Both galaxies were identified as having weak but definite spiral-arm structure in Lisker et al. (2006) and Ferrarese et al. (2006a). In addition, Lisker et al. (2006) report from SDSS imaging the possible detection of spiral arms in 9–14 (1.9%–2.9%) dwarfs in their sample of 476 early-type dEs (426 = 89%) and dS0s (50 = 11%). This result demonstrates that dwarfs as a class, the dS0s included, only rarely show evidence for spiral structure. Moreover, of the 41 dwarfs (8.6%) that are identified by Lisker et al. (2006) as showing certain, probable or possible disk features (i.e., having evidence of spiral arms, central bars, extreme flattenings, etc.), 18 are classified as dS0s, 19 as dEs, and 4 as dE or dS0s; the small number of dwarfs showing disk-like features is therefore equally likely to have been classified in the past as dE or dS0 systems.

non-nucleated varieties). Based on our imaging, there is little to distinguish quantitatively the dS0s from dEs. This is consistent with the findings of Ryden et al. (1999) who studied the surface brightness, axial ratios, and isophotal structure of 70 Virgo dwarfs (Ryden & Terndrup 1994) and concluded that “There does not seem to be any combination of parameters from the surface photometry that statistically correlates with the dE/dS0 designation: in particular, the dS0 galaxies do not, on average, have more pointed (disky) isophotes than the dEs.”

In all, the evidence from the ellipticity measurements suggests that the low-luminosity galaxies considered here have intrinsic shapes that more closely resemble those of the high-luminosity systems than is sometimes appreciated. Of course, a non-negligible fraction of bright dEs or dS0s do show disk-like features (see, e.g., Aguerri et al. 2005; Lisker et al. 2006) and some faint galaxies certainly have unmistakable disk-like structures. Nevertheless, the ACSVCS dwarfs brighter than  $M_B \simeq -15$ —which are thought to be representative of the Virgo dwarf population in this magnitude range (Côté et al. 2004)—are, as a whole, probably mildly triaxial, with individual objects spanning a wide range in internal structure from nearly spherical systems to thin disks (e.g., Binggeli & Popescu 1995; Lisker et al. 2007, Lisker et al. 2009). Indeed, the lack of sub-populations within the dwarf class would be surprising, given that different physical processes, many of which depend sensitively on environment, are expected play a role in driving their internal structure (e.g., Gunn & Gott 1972; Larson et al. 1980; Babul & Rees 1992; Moore et al. 1996).

### 3.4. The Color–Color and Color–Magnitude Relations

It is well known that the history of star formation and chemical enrichment in any stellar population is reflected in its CMR. The CMR for old stellar systems was first studied by Baum (1959) who drew attention to the importance of overall mass in driving the evolution of the stellar content of galaxies. Faber (1973b) showed that there appeared to exist a nearly universal CMR for bright, early-type galaxies (Es and S0s) in a diversity of environments. Subsequent observations in galaxies belonging to the Virgo Cluster showed that its early-type population—again, with no apparent distinction between Es and S0s—defined a narrow sequence in color, perhaps offset from the sequence defined by the late-type systems (i.e., Visvanathan & Sandage 1977; Sandage & Visvanathan 1978). The CMR for galaxies has taken on a renewed importance in recent years, with the availability of accurate colors and magnitudes for extremely large statistical samples. These studies have revealed a strongly bimodal distribution of galaxies in the color–magnitude diagram, with early-type systems defining a narrow “red-sequence” and late-type systems showing a more extended distribution (e.g., Strateva et al. 2001; Bell et al. 2004; Baldry et al. 2004, 2006). Although the CMR of *low-mass* early-type galaxies is more of an open question, early studies pointed to a roughly linear CMR (Caldwell 1983; Prugniel et al. 1993), with some evidence for a continuity with that of the highest mass, early-type systems (e.g., Secker et al. 1997; Conselice et al. 2002; Karick et al. 2003).

On the other hand, several recent studies have suggested that a single linear relation that extends from the upper end of the red sequence down to the level of low-mass “dwarf” galaxies is *not* a good description of the overall early-type CMR. Indeed, this was shown specifically in Virgo for the 100 ACSVCS galaxies by Ferrarese et al. (2006a), who fitted a quadratic relation to their ACS-based colors and magnitudes. More recently, Janz &

Lisker (2009) examined the CMR for 468 early-type galaxies in the Virgo Cluster (relying on the original morphological types of Binggeli et al. 1985) using an approach that is quite similar to the one described here: i.e., nonparametric aperture photometry performed on SDSS images. They confirmed the nonlinearity noted by Ferrarese et al. (2006a), but, thanks to the expanded magnitude coverage of their sample, found a smooth “S-shaped” distribution of galaxies in the color–magnitude plane, with an inflection between  $-19.0 \lesssim M_g \lesssim -17$  (see their Figure 1).

In Figure 17, we show CMRs in several bandpass combinations for our 100 sample galaxies. Because the different colors in Table 3 behave similarly, we show only the measurements between  $1''$  and  $R_e$  after applying de-reddening corrections based on the DIRBE maps of Schlegel et al. (1998). Absolute magnitudes,  $M_g$ , were derived using the recalibrated SBF distances from Blakeslee et al. (2009); the mean Virgo Cluster distance of 16.5 Mpc (Mei et al. 2007) was adopted for 16 galaxies without a direct distance measurement.

The smooth curve in each panel shows the locally weighted scatterplot smoothing (LOWESS) fit to each CMR (see Cleveland & McGill 1984). These non-parametric fits highlight the fact that the precise form of the CMR varies depending on the choice of the color index, but it is clearly nonlinear for a number of the color indices over the  $\approx 7$  mag range explored here. This consistent with the conclusions of Ferrarese et al. (2006a) and Janz & Lisker (2009), and contrary to the claim of a linear relation by Andreon et al. (2006). The LOWESS fits also reveal, once again in agreement with the findings of Janz & Lisker (2009) who used a larger sample that extends by  $\sim 2$  mag to fainter magnitudes, that the CMR has an approximately S-shaped form. We point out that the CMR, although nonlinear, is not *discontinuous*, extending smoothly across the region  $-19 \lesssim M_g \lesssim -17$  that separates the bulk of the galaxies classified as “dwarfs” from “giants.” In other words, there is no evidence from the stellar populations in these galaxies for a “dichotomy” between these two populations (or for that matter, for two distinct populations that uniquely map into the morphological classifications). There is, however, an apparent tendency for the faintest systems to show a larger scatter than those of intermediate luminosities. To quantify this impression, we can divide the sample into three broad bins: (1)  $M_g \leq -21.5$ ; (2)  $-21.5 < M_g \leq -18.5$ ; and (3)  $M_g > -18.5$  and focus on the  $(g-z)-M_g$  relation in panel (g) which samples a long color baseline with reasonably small errors. For galaxies in these three bins, the ratio of the rms scatter about the LOWESS relation to the mean color errors are 3.90, 1.45, and 1.84, respectively. We conclude that the increase in scatter for the faint systems compared to those of intermediate luminosity is not merely due to a rise in the photometric errors. For the brightest galaxies, one should view the apparent increase in this ratio with some caution since it is based on just seven galaxies (one of which is the post-merger remnant VCC798; see below) and depends rather sensitively on the adopted systematic/zero-point uncertainties which dominate the error budget for these bright systems.

The increased scatter for the fainter galaxies is likely due to the well-known diversity in star formation history among low-mass galaxies (see, e.g., the reviews of Mateo 1998 and Grebel 2001 and references therein). Indeed, a number of the low-mass galaxies in the sample are known from the ACS images to show dust filaments, ongoing star formation, young star clusters or associations, and/or irregular isophotes (e.g., VCC1499, 21, 1779, 1488, 1512, and 1948; Côté et al. 2006). These “dE/dIrr transition galaxies” tend to fall in a sparsely populated tail that

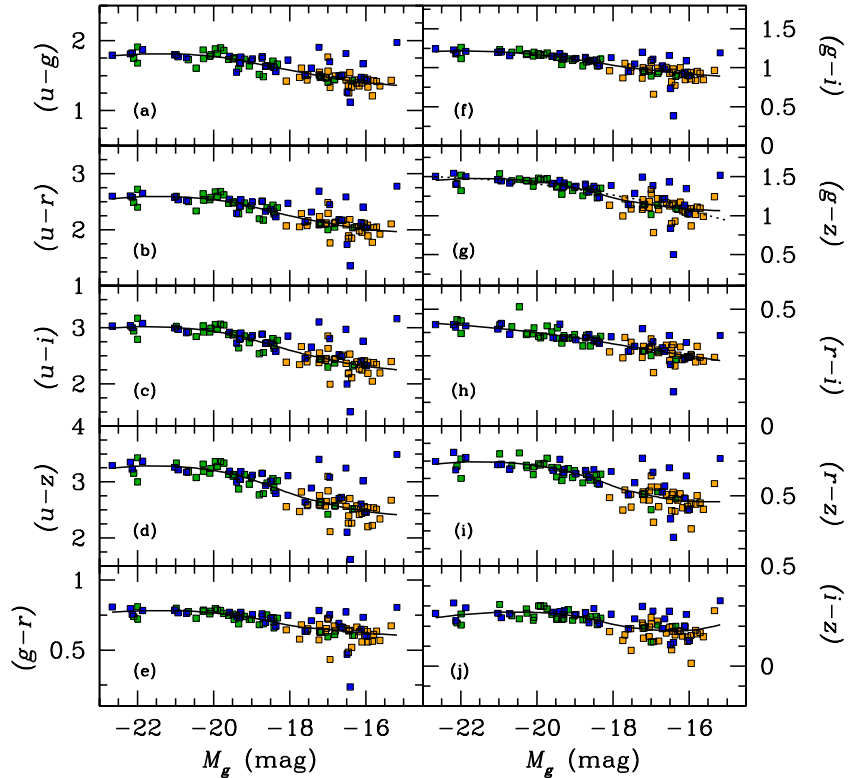


**Figure 17.** Color–magnitude relations (CMRs) for the program galaxies from the SDSS imaging. The smooth polynomial in each panel is a LOWESS (Cleveland & McGill 1984) fit to the data, highlighting the nonlinear nature of several of the CMRs; the S-shaped behavior of the CMRs reported by Janz & Lisker (2009) is apparent in a number of the panels, most notably (d), (g), (h), and (i). The dotted curve in the ( $g - z$ ) CMR shows the quadratic relation of Ferrarese et al. (2006a) after applying a small blue color shift of 0.04 mag in order to match the SDSS data; it is an adequate description of our data over this magnitude range.

extends from the faint end of the fitted polynomial relations toward bluer colors. At the same time, there is a handful of low-luminosity galaxies that extend to significantly *redder* colors. These objects, which have tended to have been classified as “E” galaxies in the past, are the same objects (VCC1297, VCC1192, VCC1627, and VCC1199) that were found to be outliers in the scaling relations and lie in close proximity to the most massive galaxies in the Virgo Cluster (Section 3.4). The red colors of these galaxies are additional evidence that tidal stripping has led to a significant reduction in their total luminosity (Faber 1973a; Bekki et al. 2001b; Côté et al. 2010; D. E. McLaughlin et al. 2010, in preparation). Finally, Figure 18 illustrates the general trends described above: i.e., a smoothly increasing diversity in the mix of stellar populations with decreasing galaxy luminosity. The left and right panels of this figure show color–color and color–magnitude diagrams for the sample galaxies compared with single-burst stellar population synthesis models from Bruzual & Charlot (2003). The models, which assume a Chabrier (2003) IMF, are shown for constant metallicity and varying age. Points along the isometallicity tracks mark ages of 1, 2, 5, 8, 10, and 12 Gyr. In the right panel, the  $g$ -band magnitudes have been normalized to total stellar masses of  $\log M_*/M_\odot = 12, 11, 10$ , and 9. This exercise demonstrates that nearly every galaxy in the sample is consistent with a mean age between 2 and 12 Gyr and mean metallicities in the range  $\approx -1.0$  to  $+0.0$  dex. At the highest masses, the implied stellar masses fall in the range of  $10^{11.5} - 10^{12}$  solar masses, with roughly solar metallicities and old ages  $T \gtrsim 10$  Gyr (although there are clear exceptions, such as VCC798 = M85, which shows significantly bluer colors consistent with a somewhat younger age; Schweizer & Seitzer 1992; Peng et al. 2006b).

The distribution of low-mass galaxies in the color–magnitude and color–color diagrams points to larger dispersions in both age ( $2 \text{ Gyr} \lesssim T \lesssim 12 \text{ Gyr}$ ) and metallicity ( $[\text{Fe}/\text{H}] = -0.7$  to  $+0.0$  dex). This is consistent with the findings of Gavazzi et al. (2002), who showed from UV-NIR spectrophotometry that the star-forming period of early-type galaxies in Virgo correlates with  $H$ -band luminosity (with low-mass systems showing more extended star formation periods).

#### 4. SUMMARY

We have carried out an analysis of the photometric and structural properties of 100 ACSVCS galaxies using homogeneous, multi-wavelength ( $ugriz$ ), wide-field imaging from the SDSS (DR5). The early-type galaxies that were targeted in this survey populate the red sequence in the Virgo Cluster and span a factor of nearly  $\sim 10^3$  in  $g$ -band luminosity. To perform our non-parametric analysis, we have developed an automated pipeline that generates background-subtracted mosaic images, masks field sources, and measures mean axial ratios, total magnitudes, effective radii, and effective surface brightnesses using a standard COG technique. We compare our results to measurements for these galaxies taken from the literature (usually determined by parametric fitting of the one-dimensional surface brightness profiles) and from the ACSVCS. We examine whether any discrepancies exist, and, if so, whether these may have arisen from the more limited field of view of the ACSVCS imaging ( $200'' \times 200''$ ). We have also carried out a parametric analysis of the surface brightness profiles by fitting Sérsic models for all galaxies and comparing the derived structural parameters, magnitudes, and mean colors to those from the ACSVCS and VCC.

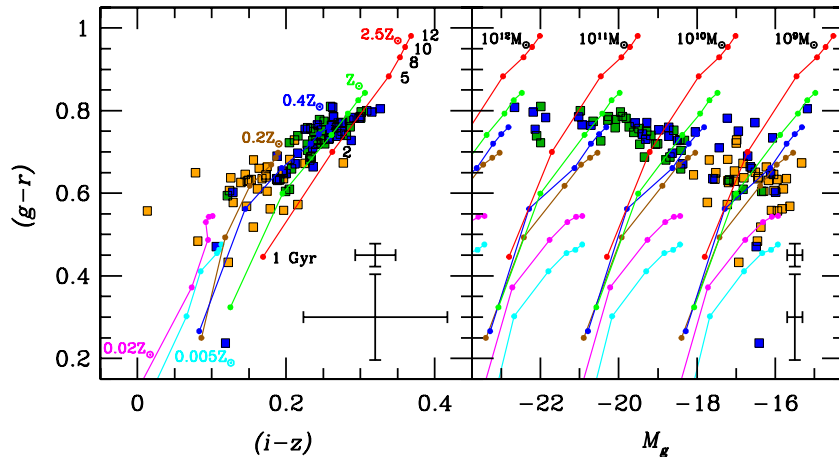


**Figure 18.** Left: color–color diagram for the program galaxies compared to the single-burst stellar population synthesis models of Bruzual & Charlot (2003). The different curves show models of constant metallicity and varying age for  $[Fe/H] = -2.3$  (cyan),  $-1.7$  (magenta),  $-0.7$  (brown),  $-0.4$  (blue),  $0$  (green), and  $+0.4$  (red). Ages of  $1$ ,  $2$ ,  $5$ ,  $8$ ,  $10$ , and  $12$  Gyr are indicated and connected along iso-metallicity lines. A Chabrier (2003) IMF has been assumed in all cases. Right: color–magnitude diagram for the program galaxies, again compared to the single-burst stellar population synthesis models of Bruzual & Charlot (2003). In this comparison, the  $g$ -band magnitudes have been normalized to total stellar masses of  $M_* = 10^{12}$ ,  $10^{11}$ ,  $10^{10}$ , and  $10^9 M_\odot$ . In each panel, the two sets of error bars in the lower right corner show the mean error for the brighter and fainter half of the sample.

(A color version of this figure is available in the online journal.)

We find good to excellent agreement between our non-parametric measurements and those from the literature and from the ACSVCS. This demonstrates that it is possible to measure the basic parameters describing the global structure of nearby early-type galaxies with quite reasonable accuracy, even using different observational material and analysis techniques (i.e., COG versus three-parameter Sérsic models). At the same time, the measurements for the largest and brightest galaxies are challenging, with discrepancies of  $\sim 30\%-40\%$  in the published effective radii being typical. Nevertheless, we find the typical errors on the total blue magnitudes from the widely used VCC to be of order  $\sigma(B_T) \approx 0.2$  mag, in agreement with the estimate of Binggeli & Cameron (1993) and Gavazzi et al. (2005; cf. Young & Currie 1998). Dividing the sample into three magnitude bins, we estimate the random errors in the VCC to be  $\approx 0.13$  mag for galaxies brighter than  $B_T = 12$ ,  $\approx 0.18$  mag for galaxies with  $12 \lesssim B_T \lesssim 14$ , and  $\approx 0.27$  mag for galaxies with  $14 \lesssim B_T \lesssim 16$ .

Although a few low-mass galaxies may show evidence for a disk-like structure, the distribution of their axial ratios is in poor agreement with that expected for a population of flattened oblate disks, despite the fact that these systems, as a whole, have roughly exponential surface brightness profiles (i.e., Sérsic indices  $n_S \sim 1$ ). From a structural point of view, the distribution of projected shapes for the low-mass (“dwarf”) systems is not dissimilar from that of the higher-mass (“giant”) galaxies, suggesting a similar distribution of *intrinsic* shapes, which likely includes mildly triaxial systems in both cases. The relationship between absolute  $g$ -band magnitude and effective radius, and mean effective surface brightness shows that the parameters vary smoothly and systematically as a function of luminosity, with clear evidence for variations in structural homology along the red sequence. There are a few notable outliers—faint, compact, high surface brightness galaxies that lie in close proximity to the giant ellipticals M87, M49, and M89, suggesting the tidal stripping has been playing an important role during the formation/evolution of these compact galaxies.

The  $ugriz$  galaxy colors show a nonlinear but smooth variation over a  $\sim 7$  mag range in absolute magnitude, as noted in previous studies. Although the CMR is nonlinear, it is not discontinuous,

and extends smoothly across the region normally taken to separate “giant” galaxies from “dwarfs.” Nevertheless, there is clear evidence for enhanced scatter in color for the faintest systems—presumably the signature of increasingly diverse star formation histories for the lowest mass galaxies.

Clearly, it is of interest to extend this work to a complete sample of Virgo Cluster members in order to understand how the CMRs and scaling relations explored here behave when one extends the sample to include “Blue Cloud” and low-luminosity systems that are absent from the present study (i.e.,  $M_g \gtrsim -15.5$ ). This will soon be possible using the NGVS (L. Ferrarese et al. 2011, in preparation), which is currently imaging a  $\approx 100$  deg $^2$  region centered on the Virgo Cluster to a point-source depth of  $g_{\text{lim}} = 25.7$  ( $M_g \approx -5.5$ ) in the  $ugriz$  bandpasses. The NGVS will yield homogeneous photometric and structural parameters, at a resolution of  $\approx 0.65$  (50 pc), for thousands of Virgo Cluster galaxies spanning more than a factor of a million in baryonic mass. Comparison of these observations to the predictions of high-resolution numerical simulations should then allow the physical processes that shaped the formation and evolution of cluster galaxies to be elucidated in significantly greater detail than is currently possible.

The authors thank the anonymous referee for many useful suggestions that improved the paper, John Blakeslee for helpful discussions, and Joachim Janz and Thorsten Lisker for sending us their SDSS catalog of photometric and structural parameters for ACSVCS galaxies. C.W.C. gratefully acknowledges support from Wen-Ping Chen, and the National Science Council (NSC96-2911-I-008-006-2 and NSC96-2112-M-008-024-MY3) and Graduate Institute of Astronomy, National Central University, Taiwan. P.C. also thanks the National Central University, Taiwan for their kind hospitality during the preparation of this paper. This publication makes use of data products from the Sloan Digital Sky Survey (SDSS). Funding for SDSS and SDSS-II has been provided by the Alfred P. Sloan Foundation, the Participating Institutions, the National Science Foundation, the US Department of Energy, the National Aeronautics and Space Administration, the Japanese Monbukagakusho, the Max Planck Society, and the Higher Education Funding Coun-



- Kormendy, J., Fisher, D. B., Cornell, M. E., & Bender, R. 2009, *ApJS*, **182**, 216
- Lambas, D. G., Maddox, S. J., & Loveday, J. 1992, *MNRAS*, **258**, 404
- Larson, R. B., Tinsley, B. M., & Caldwell, C. N. 1980, *ApJ*, **237**, 692
- Longo, G., de Vaucouleurs, A., & Corwin, H. 1983, General Catalogue of Photoelectric Magnitudes and Colors in the UVB System of 3578 Galaxies Brighter than 16th V Magnitude, (1936-1982) (Austin, TX: Univ. Texas)
- Lisker, T., & Fuchs, B. 2009, *A&A*, **501**, 429
- Lisker, T., Grebel, E. K., & Binggeli, B. 2006, *AJ*, **132**, 497
- Lisker, T., Grebel, E. K., Binggeli, B., & Glatt, K. 2007, *ApJ*, **660**, 1186
- Lisker, T., et al. 2009, *ApJ*, **706**, 124
- Lotz, J. M., Miller, B. W., & Ferguson, H. C. 2004, *ApJ*, **613**, 262
- Mateo, M. L. 1998, *ARA&A*, **36**, 435
- McDonald, M., Courteau, S., & Tully, R. B. 2009, *MNRAS*, **394**, 2022
- McLaughlin, D. E. 1999, *ApJ*, **512**, 9
- Mei, S., et al. 2005a, *ApJS*, **156**, 113
- Mei, S., et al. 2005b, *ApJ*, **625**, 121
- Mei, S., et al. 2007, *ApJ*, **655**, 144
- Michard, R. 1985, *A&AS*, **59**, 205
- Michard, R. 1994, *A&A*, **288**, 401
- Mieske, S., et al. 2006, *ApJ*, **653**, 193
- Milosavljević, M., & Merritt, D. 2001, *ApJ*, **563**, 34
- Misgeld, I., Hilker, M., & Mieske, S. 2009, *A&A*, **496**, 683
- Misgeld, I., Mieske, S., & Hilker, M. 2008, *A&A*, **486**, 697
- Moore, B., Katz, N., Lake, G., Dressler, A., & Oemler, A. 1996, *Nature*, **379**, 613
- Peng, C. Y., Ho, L. C., Impey, C. D., & Rix, H. W. 2002, *AJ*, **124**, 266
- Peng, E., et al. 2008, *ApJ*, **681**, 197
- Peng, E. W., et al. 2006a, *ApJ*, **639**, 95
- Peng, E. W., et al. 2006b, *ApJ*, **639**, 838
- Petrosian, V. 1976, *ApJ*, **209**, L1
- Poulain, P. 1988, *A&AS*, **72**, 215
- Price, J., et al. 2009, *MNRAS*, **397**, 1816
- Prugniel, P., Bica, E., & Alloin, D. 1992, in Morphological and Physical Classification of Galaxies, ed. G. Longo, M. Capaccioli, & G. Busarello (Astrophys. Space Sci. Lib. 178; Dordrecht: Kluwer), 261
- Prugniel, P., Bica, E., Klotz, A., & Alloin, D. 1993, *A&AS*, **98**, 229
- Prugniel, P., & Heraudeau, P. 1998, *A&AS*, **128**, 299
- Prugniel, P., & Simien, F. 1997, *A&A*, **321**, 111
- Reaves, G. 1983, *ApJS*, **53**, 375
- Rines, K., & Geller, M. J. 2008, *AJ*, **135**, 1837
- Rix, H.-W., & White, S. D. M. 1990, *ApJ*, **362**, 52
- Rix, H.-W., & White, S. D. M. 1992, *MNRAS*, **254**, 389
- Ryden, B. S., & Terndrup, D. M. 1994, *ApJ*, **425**, 43
- Ryden, B. S., Terndrup, D. M., Pogge, R. W., & Lauer, T. R. 1999, *ApJ*, **517**, 650
- Sandage, A., & Binggeli, B. 1984, *AJ*, **89**, 919
- Sandage, A., Binggeli, B., & Tammann, G. A. 1985, *AJ*, **90**, 1759
- Sandage, A., Freeman, K. C., & Stokes, N. R. 1970, *ApJ*, **160**, 831
- Sandage, A., & Visvanathan, N. 1978, *ApJ*, **225**, 742
- Saviane, I., & Jerjen, H. 2007, *AJ*, **133**, 1756
- Schindler, S., Binggeli, B., & Bohringer, H. 1999, *A&A*, **343**, 420
- Schlegel, D. J., Finkbeiner, D. P., & Davis, M. 1998, *ApJ*, **500**, 525
- Schombert, J. M. 1986, *ApJS*, **60**, 603
- Schweizer, F., & Seitzer, P. 1992, *AJ*, **104**, 1039
- Secker, J., Harris, W. E., & Plummer, J. D. 1997, *PASP*, **109**, 1377
- Sérsic, J. L. 1968, in Atlas de Galaxias Australes, (Córdoba: Obs. Astron., Univ. Nac. Córdoba)
- Sivakoff, G. R., et al. 2007, *ApJ*, **660**, 1246
- Strateva, I., et al. 2001, *AJ*, **122**, 1861
- Tollerud, E. J., Bullock, J. S., Graves, G. J., & Wolf, J. 2010, arXiv:1007.5311
- Tonry, J. L., Dressler, A., Blakeslee, J. P., Ajhar, E. A., Fletcher, A. B., Luppino, G. A., Metzger, M. R., & Moore, C. B. 2001, *ApJ*, **546**, 681
- Trujillo, I., Erwin, P., Asensio Ramos, A., & Graham, A. W. 2004, *AJ*, **127**, 1917
- van den Bergh, S. 1994, *AJ*, **107**, 153
- van der Wel, A., Rix, H., Holden, B. P., Bell, E. F., & Robaina, A. R. 2009, *ApJ*, **706**, L120
- Visvanathan, N., & Sandage, A. 1977, *ApJ*, **216**, 214
- West, A. A., Garcia-Appadoo, D. A., Dalcanton, J. J., Disney, M. J., Rockosi, C. M., Ivezić, Z., Bentz, M. C., & Brinkmann, J. 2010, *AJ*, **139**, 315
- Wolf, J., Martinez, G. D., Bullock, J. S., Kaplinghat, M., Geha, M., Muñoz, R. R., Simon, J. D., & Avedo, F. F. 2010, *MNRAS*, **406**, 1220
- York, D. G., et al. 2000, *AJ*, **120**, 1579
- Young, C. K., & Currie, M. J. 1998, *A&AS*, **127**, 367
- Zaritsky, D., Gonzalez, A. H., & Zabludoff, A. I. 2006a, *ApJ*, **642**, L37
- Zaritsky, D., Gonzalez, A. H., & Zabludoff, A. I. 2006b, *ApJ*, **638**, 725
- Zaritsky, D., Zabludoff, A. I., & Gonzalez, A. H. 2008, *ApJ*, **682**, 68